X-band linac design

M. S. Sullivan*
Department of Physics and Astronomy, The University of Manchester, Oxford Road, Manchester, M13 9PL, United Kingdom and Cockcroft Institute, Sci-Tech Daresbury, Keckwick Lane, Daresbury, Warrington, WA4 4AD, United Kingdom

R. M. Jones
University of Manchester, Manchester, United Kingdom and Cockcroft Institute, Sci-Tech Daresbury, Keckwick Lane, Daresbury, Warrington, WA4 4AD, United Kingdom

L. S. Cowie, A. D. Brynes, and P. H. Williams
ASTeC, STFC Daresbury Laboratory, Daresbury, Warrington, WA4 4AD Cheshire, United Kingdom and Cockcroft Institute, Sci-Tech Daresbury, Keckwick Lane, Daresbury, Warrington, WA4 4AD, United Kingdom

K. Yokoya
Accelerator Laboratory, High Energy Accelerator Research Organization, 1-1 Oho, Tsukuba, Ibaraki 305-0801, Japan

(Received 14 May 2021; accepted 8 July 2021; published 10 August 2021)

In order to explore physics in the EUV to soft x-ray region, we have designed a machine which is capable of accelerating a ∼250 pC electron bunch to an energy of ∼1 GeV. The front end of the CLARA (Compact Linear Accelerator for Research and Applications) system at Daresbury Labs will be used as an S-band injector of ∼180 MeV/c, sub-ps FWHM, ∼250 pC electron bunches into the XARA (X-Band Accelerator for Research and Application) system. A rf feasibility study has been carried out for a structure operating in the $2\pi/3$ mode at a frequency of 11.9942 GHz which is fed by a SLED klyston setup. The average cell of this structure has an iris radius of $\langle a \rangle = 3.2$ mm and a shunt impedance of $\langle R_s \rangle = 106.55$ MΩ/m. A high target gradient of 80 MV/m for a single-bunch operation of the linac is necessary due to spatial constraints at Daresbury Labs. We have also implemented Gaussian detuning of the linac in order to future-proof the project for potential multibunch operation of the machine. After combining the rf study with an analysis of the uncoupled long-range wakefield and the short-range transverse wakefields, the optimal structure parameters are outlined as a compromise between the shunt impedance, electrical breakdown rate and wakefields in the structure. As novel designs will be tested using this free-electron laser (FEL) an increased beam charge may be useful. Therefore a beam dynamics study via the particle tracking code ELEGANT has been performed to assess how the beam quality evolves while traveling through the XARA rf structures for different bunch charges and beam offsets. These simulations reveal how the bunch is disturbed for varying bunch charges and offsets and give an initial indication of how sensitive the beam parameters (beam centroid position, emittance, RMS beam size, etc.) are to the wakefields generated in XARA. An analytical formulation of the beam motion as it travels through the XARA linac has been utilized to calculate the emittance growth. This allows for comparison between analytical and numerical simulation of the beam dynamics to give confidence in the results. The beam dynamics study shows that for a bunch charge of $Q_b = 250$ pC and a beam offset of $C_x = \sigma_z/2 = 0.253$ mm, the normalized emittance growth at the end of the XARA linac is $\Delta\epsilon_{Nx}/\epsilon_{Nx} \sim 270\%$. This may be mitigated by the design of a magnetic lattice which would include kickers to recenter the beam on the electrical axis of the structure, reducing the effect of the wakefields on the bunch. Currently it is probable that a maximum bunch charge of ∼250 pC will be utilized for this machine; however a future design of a magnetic focusing lattice may allow higher charges to be viable and will reduce the emittance growth.

DOI: 10.1103/PhysRevAccelBeams.24.082001

*michael.sullivan@postgrad.manchester.ac.uk

I. INTRODUCTION

The Compact Linear Accelerator for Research and Applications (CLARA) facility at Daresbury Laboratory is a project with the aim to become a Free Electron Laser (FEL) test facility. When complete, CLARA will produce an electron beam of up to 250 MeV/c, ∼250 pC charge bunches of femtosecond order length [1]. The XARA concept is to offer a potential upgrade to the existing CLARA system to create a compact accelerator capable of producing a ∼1 GeV/c electron beam which could then be used to test an increased range of novel acceleration techniques. With the XARA upgrade the FEL would be able to generate attosecond light pulses in the EUV to soft x-ray region for use in future studies of ultra-fast dynamics [2]. The CLARA project is currently supported up to phase 2 which will provide the 250 MeV/c beam and the full energy beam extraction (FEBE) line which will enable user experiments and technology demonstrations utilising the electron beam directly. Outlined in the UK XFEL Science Case [3], CLARA phase 3 includes the addition of the FEL line which would be used to demonstrate novel FEL schemes for later implementation in the UK XFEL. The CLARA front-end of phase 2 can be used as an S-Band injection line (sans linac 4) to the proposed XARA system and XARA can be considered as an alternative or future upgrade to the existing facility. This S-band injector will provide a ∼180 MeV/c (not the full ∼250 MeV/c due to the removal of linac 4), sub-ps FWHM, ∼250 pC electron beam which can be accelerated by an *X*-band linac. This would enhance the momentum of the electron beam that could be extracted by the FEBE line to ∼600 MeV/c. Only a ∼600 MeV/c beam can be extracted by the FEBE line instead of the full ∼1 GeV/c beam due to space limitations in the accelerator hall causing the point of beam extraction to be before the end of the XARA linac system. The front-end of CLARA (consisting of the gun and first linac) has been commissioned with a 2.5 cell, 10 Hz repetition (rep) rate gun, while a 1.5 cell, 400 Hz rep rate cavity will be commissioned soon [4]. Phase 2 of the CLARA facility, consisting of linacs 2, 3 and 4, an *X*-band linearizer and variable bunch compressor is currently being assembled and will be commissioned in the next few years.

This preliminary rf design of an *X*-band linac structure for XARA is based on that of the CompactLight [5] and EuPRAXIA@SPARC_LAB [6] projects, with 3 or 4 modules each supplied by one or two 50 MW *X*-band klystrons, a low loss waveguide and a SLAC energy doubler (SLED) type pulse compressor [7]. Two options have been proposed for XARA, a single bunch and a multibunch operation. The single bunch regime requires a very high accelerating gradient of ∼80 MV/m to ensure a beam momentum of ∼1 GeV/c can be achieved within 3 modules. Due to the space available for the XARA project, the gradient will be prioritized even if two klystrons are required over one. The multibunch regime will require a longer rf pulse or shorter cavities to reduce the filling time of the structure. The short wavelength required for an *X*-band structure gives rise to strong geometric wakefields due to the transverse size of the structure decreasing to support a traveling wave of the correct phase velocity. Therefore the irises are located closer to the beam, increasing the strength of the wakefields [8]. These transverse wakefields can strongly deteriorate the quality of the beam. To this end, linacs with both linear and Gaussian tapered irises down the structure have been considered in order to reduce the magnitude of the wakefields. It is also possible to reduce further the wakefields by widening the iris thickness in a future design. Variation of the iris thickness down the structure results in a detuning of the synchronous frequency of the lowest dipole modes. This causes a decoherence in the transverse wakefields and thus a suppression of their amplitude [9–11]. This option has not been explored in this study as multibunch operation is not currently planned for the XARA system. However, if long-range transverse wakes prove problematic in the future, the design could expand to include tapering of the iris thickness.

In this paper a base rf design for the XARA *X*-band linac has been outlined which operates at a frequency of 11.9942 GHz in the $2\pi/3$ mode. First, the single cell parameters have been calculated via High Frequency Structure Simulator [12] (HFSS) electromagnetic simulations and interpolated over a range of iris radii. This allows the gradient profile along the structure to be found using the electric fields produced by a SLED pulse as well as determining if the structure exceeds given breakdown limits. This is done for multiple lengths of structure and tapering. Once the behavior of the iris radii down the linac is known, the long-range wakefields are calculated via summation of synchronous parameters, i.e. parameters of modes which interact with and are "synchronous" with the beam. The short-range wakefields are calculated via a field-matching technique with complex frequency. To assess how destructive the short-range wakefields are on the quality of the beam, beam dynamics simulations are carried out via the ELEGANT particle tracking code [13] as the beam travels through a full rf structure where the desired final beam energy is achieved. Manual calculations of the Twiss parameters of the beam are carried out using the final phase space and compared to output found by ELEGANT to good agreement. These results are then compared to an analytical description of emittance dilution due to short-range wakefields acting on bunches of short lengths. Together, these studies allow for restrictions to be placed on the amount of charge within an accelerated bunch in consideration of an allowed emittance dilution over the whole structure.

II. SINGLE CELL STUDY

A. Monopole mode

The EuPRAXIA structure [14] as shown in Fig. 1 has formed a starting point in the design of the *X*-band

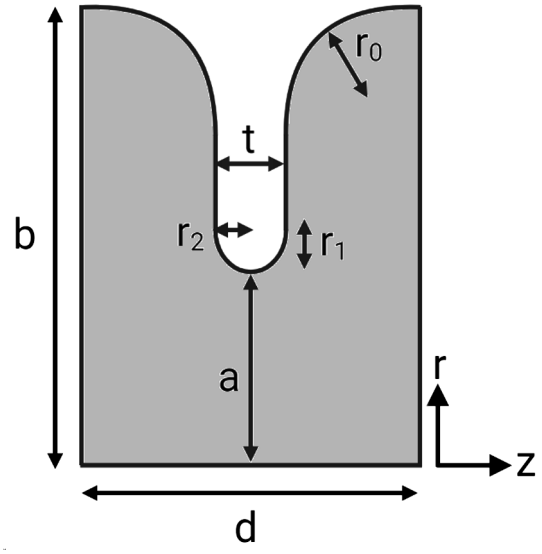

FIG. 1. The general geometry of the cell design with parameters labeled. The electron beam travels from left to right along the z-axis, i.e. $r = 0$.

structure. During the design of the geometry, the main considerations were to maximize the shunt impedance per unit length R' and minimize the modified Poynting vector [15] normalized to the average accelerating gradient squared S_{cmax}/E_{acc}^2 which will allow for a higher gradient while reducing the breakdown rate. The initial design selects an average radius of $\langle a \rangle = 3.2$ mm for the structure. Simulations were carried out via ANSYS HFSS [12] to calculate the $2\pi/3$ mode of the cell for a range of iris radii a, adjusting the cell radii b such that the operating mode frequency $\omega/2\pi = 11.9942$ GHz is synchronous with the beam. The operational $2\pi/3$ mode was chosen as a compromise between the cell length due to space limitations and a high group velocity which is required for

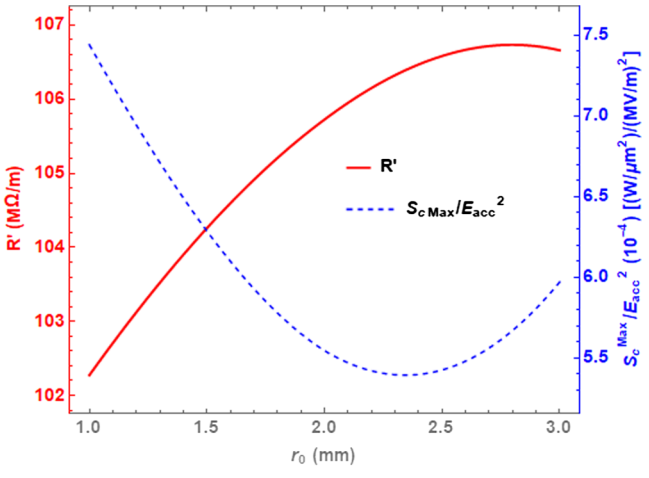

FIG. 2. The shunt impedance per unit length R' and the normalized modified Poynting vector S_c/E_{acc}^2 as a function of the cell rounding radius r_0 for iris radius $a = 3.2$ mm.

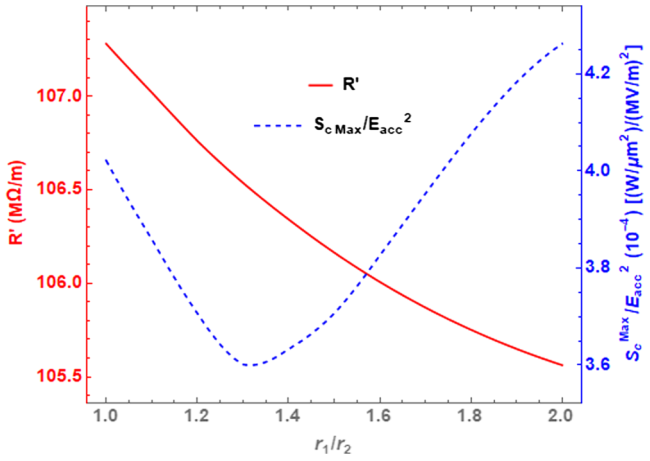

FIG. 3. The shunt impedance per unit length R' and the normalized modified Poynting vector S_c/E_{acc}^2 as a function of the elliptical iris radii ratio r_1/r_2 for iris radius $a = 3.2$ mm.

efficient acceleration of the beam [16]. Initially, simulations were done to establish optimal values for the cell rounding radius r_0 and the ratio of the elliptical radii r_1/r_2 with their effects on R' and S_{cmax}/E_{acc}^2 given in Figs. 2 and 3 respectively. The values $r_0 = 2.5$ mm and $r_1/r_2 = 1.3$ were chosen as a compromise to maximize and minimize R' and S_{cmax}/E_{acc}^2 respectively. Once the values for r_0 and r_1/r_2 are decided, dispersion relationships for a range of iris radii a are calculated. The corresponding cell radii b are calculated to tune the cell frequency to the operating frequency. The following cell parameters can be found via HFSS: the quality factor Q which characterizes rf losses in the cavity, the group velocity v_g, the R' and S_{cmax}/E_{acc}^2. The monopole dispersion which describes the coupling between the rf cell and the beam is defined as [17,18]

$$\omega = \frac{\omega_{\pi/2}}{\sqrt{1 + \kappa \cos\phi}}, \tag{1}$$

where $\omega = 2\pi f$ is the angular frequency with f being the frequency and ϕ is the phase advance of a cell. The frequency of the $\pi/2$ mode $\omega_{\pi/2}$ and the coupling κ are given by

$$\omega_{\pi/2} = \sqrt{\frac{2\omega_0^2\omega_\pi^2}{\omega_0^2 + \omega_\pi^2}}, \tag{2}$$

$$\kappa = \frac{\omega_\pi^2 - \omega_0^2}{\omega_0^2 + \omega_\pi^2}, \tag{3}$$

where the frequencies of the 0 and π modes can be calculated via most electromagnetic simulation programs, where in this case HFSS has been used. The monopole dispersion relations are shown in Fig. 4 for rf cells with a range of a. As the beam moves through the cavity, it will

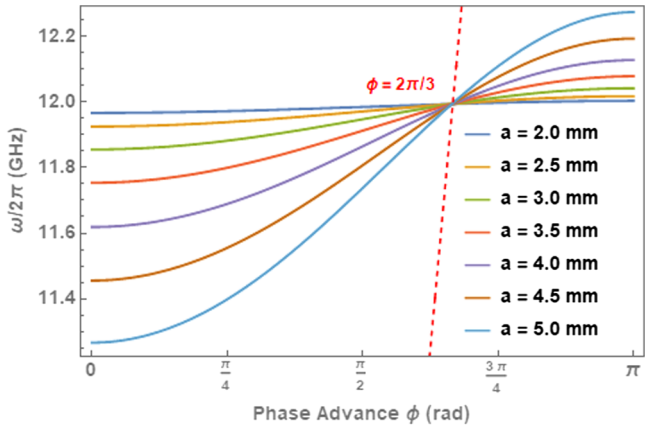

FIG. 4. The accelerating monopole dispersions for the base XARA cell for varying iris radii where the operating $2\pi/3$ mode is tuned to 11.9942 GHz. The light line (LL) which represents the phase velocity of light is shown in dashed red.

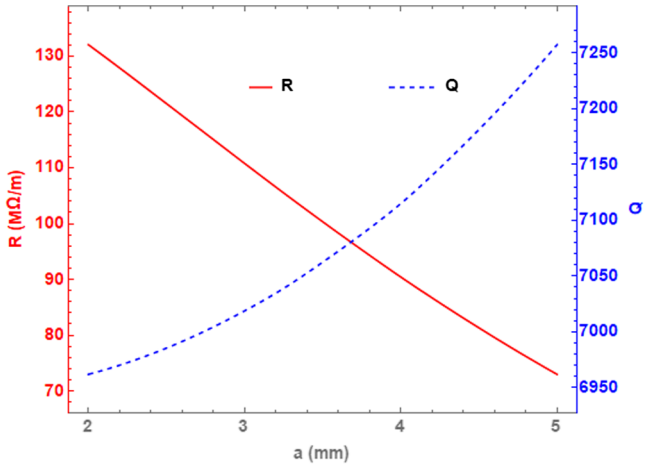

FIG. 5. The shunt impedance per unit length R' and Q factor of the single cell tuned to 11.9942 GHz in the $2\pi/3$ mode as a function of cell iris radius a.

excite in principle an infinite number of modes. However, it will strongly excite the mode which is synchronous with the speed of light. This mode is excited coherently while all other modes of the dispersion relation will constructively and destructively interfere as they all have different phase velocities. The synchronous mode is indicated by the intersect between the dispersion relation and the "light line" (LL) which represents the phase velocity of light. This synchronous mode is coherently excited and all of the modes superimpose to give a much stronger effect than any of the other modes which average to zero [17,18]. In this design, all cells are tuned such that operating $2\pi/3$ mode intersects the LL. The cell parameters are found using the HFSS fields calculator using the following definitions [14]:

$$V_{acc} = \int_0^{L_c} E_z \exp\left(\frac{i\omega z}{\beta c}\right) \mathrm{d}z, \tag{4}$$

$$W = \frac{\epsilon_0}{2}\int_{V_c} |E|^2 \mathrm{d}V = \frac{\mu_0}{2}\int_{V_c} |H|^2 \mathrm{d}V, \tag{5}$$

$$Q = \frac{\Re(\omega)}{2\Im(\omega)}, \tag{6}$$

$$R' = \frac{Q|V_{acc}|^2}{\omega W L_c}, \tag{7}$$

$$\frac{S_{cmax}}{E_{acc}^2} = \frac{\max(\Re(S) + \frac{1}{6}\Im(S))}{(V_{acc}/L_c)^2}, \tag{8}$$

where V_{acc} is the accelerating voltage per period, L_c is the cell length, E_z is the axial electric field parallel to the beam, z is the direction parallel to the beam motion, $\beta = v/c$ where v is the beam velocity and c is the speed of light in a vacuum, W is the stored electromagnetic energy in the cell, V_c is the cell volume, ϵ_0 is the permittivity of free space, μ_0 is the permeability of free space and S is the Poynting vector. Equation (5) shows that the time-averaged electrical stored energy per period is equal to the time-averaged magnetic stored energy per period for an rf cavity at resonance. For this study, it is assumed that $\beta = 1$. Using these definitions along with the monopole dispersion relations, the cell parameters are calculated and are shown in Figs. 5 and 6. The values for the single cell with $a =$ 3.2 mm are given in Table I.

In this paper both linear and Gaussian tapering of the iris radii will be considered to maximize the shunt impedance per unit length R' which describes the ability of an rf cell to support the voltage necessary to accelerate the beam efficiently. However, this also has an effect on the strength of the geometric wakefields in the structure described by the behavior of the dipole modes.

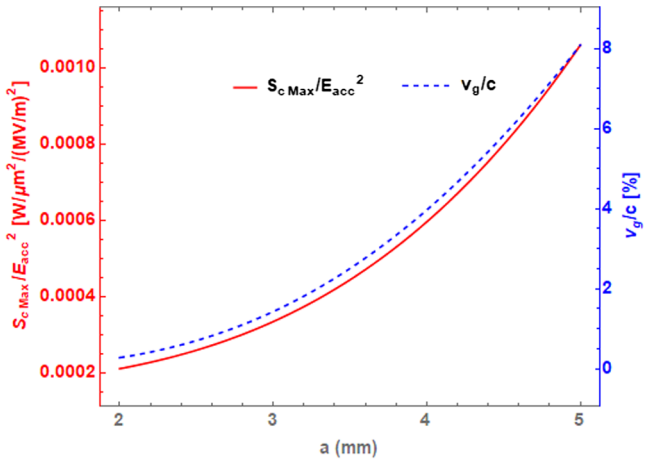

FIG. 6. The maximum modified Poynting vector normalized to the square of the accelerating electric field S_c/E_{acc}^2 and group velocity v_g/c of the single cell tuned to 11.9942 GHz in the $2\pi/3$ mode as a function of iris cell a.

TABLE I. Optimized rf structure parameters for a representative single cell with $a = 3.2$ mm.

Parameter	Value
Iris radius a (mm)	3.2
Cell radius b (mm)	10.454
Iris thickness t (mm)	2.0
Cell length L_c (mm)	8.332
$\langle a \rangle/\lambda$	0.128
r_0 (mm)	2.5
r_2 (mm)	1.0
r_1/r_2	1.3
R' (MΩ/m)	106.55
v_g/c (%)	1.81
Quality factor Q	7034
S_{cmax}/E_{acc}^2 (W/μm^2/(MV/m)^2)	3.74×10^{-4}

B. Dipole modes

Electromagnetic simulations have been carried out in HFSS to calculate the 0 and π mode frequencies of the lowest dipole mode for the rf cells. This allows the dispersion relation of the dipole modes to be calculated via Eq. (1). The dipole dispersions are presented in Fig. 7. While the monopole dispersions of the rf cells intersect with the LL at phase advance $\phi = 2\pi/3$, the same is not true of the dipole modes. Hence the dipole modes interact with the beam at different phase advances and frequencies which depend on the iris radii a of the cell. To describe how the dipole modes that will interact with the electron beam are distributed along the structure, the synchronous frequencies are found as a function of the iris radii as shown in Fig. 8. A cubic interpolation of these values allow the synchronous frequencies to be found for intermediate values of the iris radii.

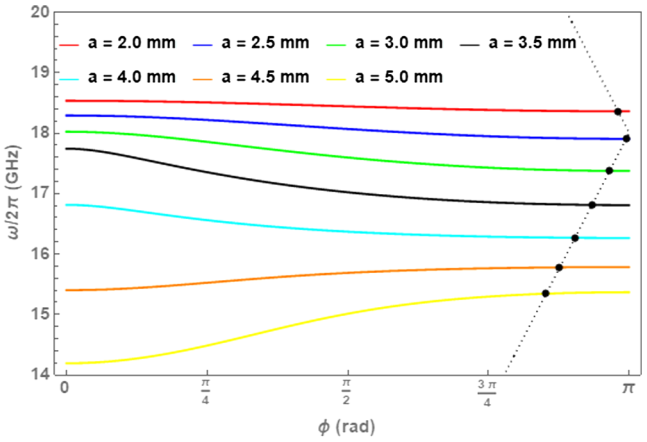

FIG. 7. The lowest dipole mode dispersion relations for a range of iris radii a where the light line (the modes that are synchronous with the beam) is shown with a dotted line. The synchronous dipole frequencies are shown as black dots.

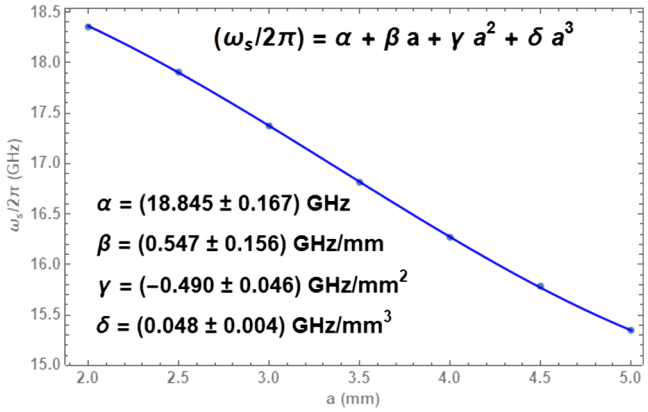

FIG. 8. The synchronous dipole frequencies as a function of the cell radii a. The dots are values found via HFSS simulations and the solid line is the cubic fit.

To understand the mode spectrum of the deflecting modes the kick factors K_s of the synchronous dipole modes are calculated in HFSS [12] and corroborated by the code TRANSVRS [19]. This is done by studying how the accelerating voltage $V_{acc,n}(r)$ falls off with transverse offset r from the electrical axis of the cell. The longitudinal loss parameter and the transverse kick factor are related by [17]

$$k_{||,n}(r) = \frac{|V_{acc,n}(r)|^2}{4W_n}, \tag{9}$$

$$K_n = \frac{c}{2L_c}\frac{R_{s,n}}{Q_n} = \frac{k_{||,n}c}{\omega_n r^2 L_c}, \tag{10}$$

where for mode n, $k_{||,n}(r)$ is the longitudinal loss factor, K_n is the transverse kick factor, W_n is the total energy stored in the cell, $R_{s,n}$ is the shunt impedance and Q_n is the Q-factor. The main parameters of the lowest dipole modes are given in Table II.

TABLE II. The iris radii a, cell radii b, synchronous dipole frequency $\omega_s/2\pi$ and the synchronous dipole kick K_s for seven fiducial cells of the XARA X-band structure. Intermediate values can be interpolated using this table.

Cell label	a (mm)	b (mm)	$\omega_s/2\pi$ (GHz)	K_s (MV/(pC m mm))
A	2.0	10.157	18.360	106.0
B	2.5	10.258	17.905	89.4
C	3.0	10.392	17.375	77.9
D	3.5	10.555	16.812	64.9
E	4.0	10.749	16.268	52.4
F	4.5	10.969	15.779	41.5
G	5.0	11.220	15.344	32.5

III. NUMERICAL OPTIMIZATION OF STRUCTURE

A. SLED parameters

In a constant gradient (CG) structure, the profile of the accelerating electric field is constant along the structure. Typically, in order to have a closed form of the solution, both R and Q are constant along z. However, the SLED type pulse compressor produces a nonflat rf pulse, leading to a nonconstant gradient profile [7]. To calculate accurately the gradient profile of the structure, a numerical optimization scheme is utilized via Wolfram *Mathematica* [20] to interpolate the rf parameters along the structure. The SLED system consists of two main components: a 180 degrees phase shifter and two overcoupled cavities of Q-factor Q_0, which store the incoming rf power, on the output side with a 3 dB coupler. The 3 dB coupler prevents any energy from being reflected back toward the klystron. After the rf pulse is phase shifted at time t_1, the stored rf power is emptied from the cavities and combined with the shifted incoming rf wave to increase the power flow toward the accelerator. The total length of the klystron pulse is given by $t_2 = t_1 + t_f$ where t_f is the filling time of the structure.

The SLED output pulse profile can be calculated by considering the combination of the electric fields before the klystron phase switch at t_1, between the klystron switch and the end of the pulse at t_2, and after the klystron pulse [14]. The resulting pulse profile is shown in Fig. 9.

As a guideline, the effective shunt impedance R_s of a CG structure is considered.

$$\frac{R_s}{R_{s,c}} = (1-\exp(-2\tau_s))\left[\gamma\exp(-Q\tau_s/Q_l) \times \frac{1-(\exp(-2\tau_s))^{1-Q/2Q_l}}{(1-Q/2Q_l)(1-\exp(-2\tau_s))} - (\alpha-1)\right]^2, \quad (11)$$

$$\gamma = \alpha\left(2-\exp\left(-\frac{t_1\omega}{2Q_l}\right)\right), \quad (12)$$

$$\alpha = \frac{2Q_0/Q_e}{1+Q_0/Q_e}, \quad (13)$$

$$\tau_s = \frac{1}{2}\int_0^{L_s}\frac{\omega}{v_g(z)Q(z)}\mathrm{d}z, \quad (14)$$

where $R_{s,c}$ is the shunt impedance of a single cell (which is assumed constant) and Q_0 is the unloaded quality factor of the overcoupled SLED cavities which has been set to 180,000, Q_e is the external SLED quality factor, $Q_l = Q_0/(1+Q_0/Q_e)$ is the loaded SLED quality factor and τ_s is the section attenuation [7]. It is worth noticing that the effective shunt impedance is a sole function of τ_s and Q_e. The numerical tool implements Eqs. (11) to (14) to find the optimum value for Q_e, an example of which is shown in Fig. 10. Once the optimal Q_e is found, the optimal τ_s can be discovered, as shown in Fig. 11. Once the optimal values for R_s, τ_s, and Q_e are found, the optimal structure length can be found by $L_s = v_g Q\tau_s/\omega$ and the filling time by $t_f = 2Q\tau_s/\omega$ [14]. R' and Q are taken constant along the structure where the single cell parameters with $\langle a\rangle = 3.2$ mm are used. The optimal parameters of such a constant gradient structure are given in Table III.

After one filling time, the distribution of the accelerating gradient along the structure is given by [21,22]

$$G(z, t=t_f) = G_0[t_f - \tau(z)]g(z), \quad (15)$$

$$G_0(t) = \sqrt{\frac{\omega R'(0)}{v_g(0)Q(0)}}P_k E_{\mathrm{out}}(t+t_1), \quad (16)$$

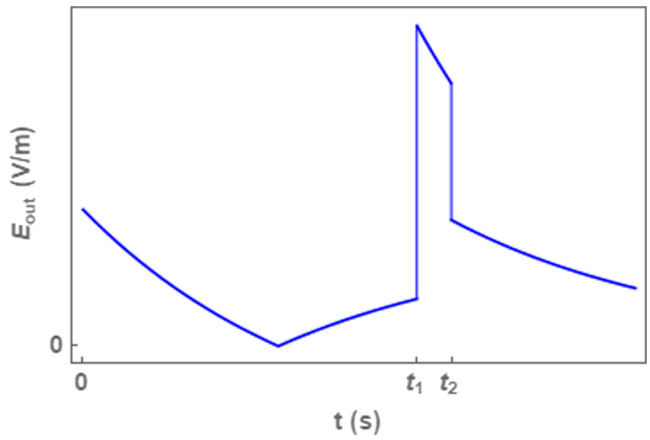

FIG. 9. The output rf pulse profile from the SLED system which increase the power flow toward the accelerator. The klystron is phase shifted by 180 degrees at time t_1 and the total length of the klystron pulse is given by t_2.

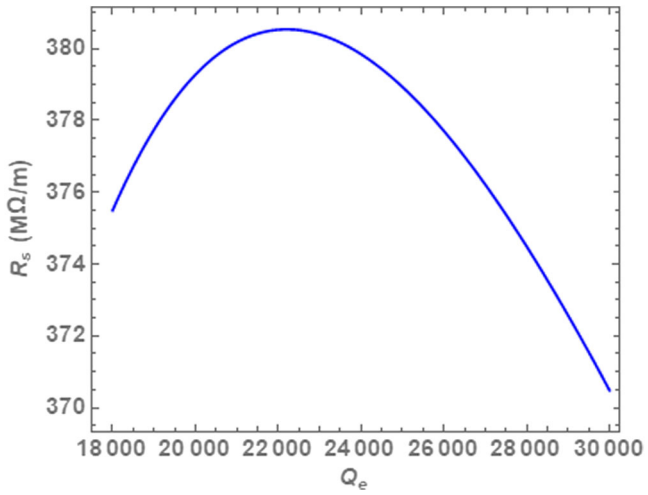

FIG. 10. The effective shunt impedance per unit length R_s of a CG structure as a function of the external SLED quality factor Q_e.

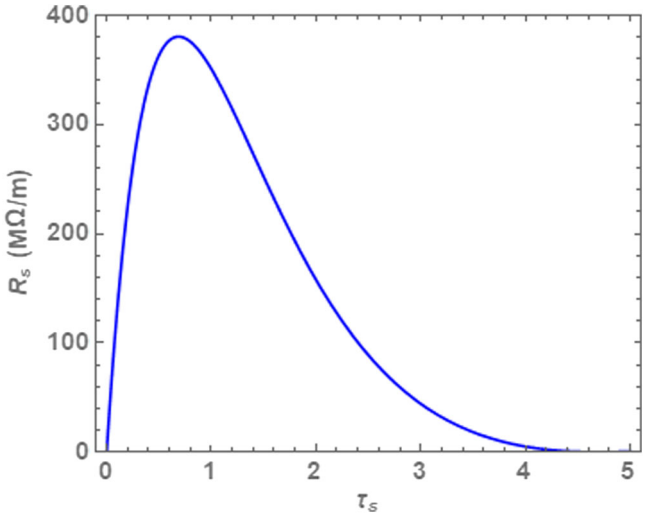

FIG. 11. The shunt impedance per unit length of a CG structure as a function of the section attenuation τ_s.

$$g(z) = \sqrt{\frac{v_g(0)}{v_g(z)}}\sqrt{\frac{R'(z)Q(0)}{R'(0)Q(z)}} \times \exp\left(-\frac{1}{2}\int_0^z \frac{\omega}{v_g(z')Q(z')}\mathrm{d}z'\right), \quad (17)$$

$$\tau(z) = \int_0^z \frac{1}{v_g(z')}\mathrm{d}z', \quad (18)$$

where P_k is the klystron output power, E_{out} is the electric field output from the SLED system and τ is the signal delay.

Due to the nonflat pulses from the SLED system, the analytical CG formulas are an approximation. Also, these formulas allow for the optimal length of the structure to be calculated, although for real accelerators there are often space limitations. Therefore it becomes apparent that a tool is needed to calculate the main rf parameters for a fixed length. This has been done for both structures where the iris variation through the structure is linear with a fixed tapering angle θ and a structure where the tapering is Gaussian with a fixed standard deviation σ and frequency spread $\Delta\omega$.

B. Linear taper

The simplest method of varying the iris radii along the structure is a linear taper where the average radius is fixed at $\langle a \rangle = 3.2$ mm. The gradient profile (15) is calculated for a range of radius tapering angle θ and structure lengths L_s and are illustrated in Fig. 12. The structure parameters for each cell in the structure are found by an interpolation of the plots shown in Figs. 5 and 6. The modified Poynting vector [15] is calculated by multiplying the square of the peak electric field $E_{\text{out}}^2(t=0)$ by the normalized S_{cmax}/E_{acc}^2 as the pulse travels through the structure. As the electrical breakdown is related to the maximum electromagnetic fields in the structure, it is important to consider the maximum modified Poynting vector. S_c is a parameter that describes a model of the electrical breakdown trigger in which the field emission currents from potential breakdown sites cause local pulsed heating. The S_c takes into account both active and reactive vector power flow on the surface structure [15]. S_c as a function of the iris tapering angle θ is shown in Fig. 13. The main restriction on the gradient in accelerator structures is the vacuum rf breakdown. The generally accepted breakdown limit parameters for an X-band structure are for a breakdown rate (BDR) of 10^{-6} breakdowns per pulse per meter (bpp/m), S_c and the pulse length t_p should not exceed 4 W/μm^2 and 200 ns respectively [15]. In order to guarantee good performance of the accelerator, the parameters must be kept under these thresholds guided by the scaling law

$$\frac{S_c^2 t_p}{BDR^{1/5}} = \text{const.} \quad (19)$$

The maximum modified Poynting vector of the structure and its corresponding breakdown limit for a range of

TABLE III. Optimal CG structure parameters using analytical expressions (11)–(14).

Parameter	Value
R_s [MΩ/m]	380.54
Filling time t_f [ns]	129
Q_e of SLED	22207

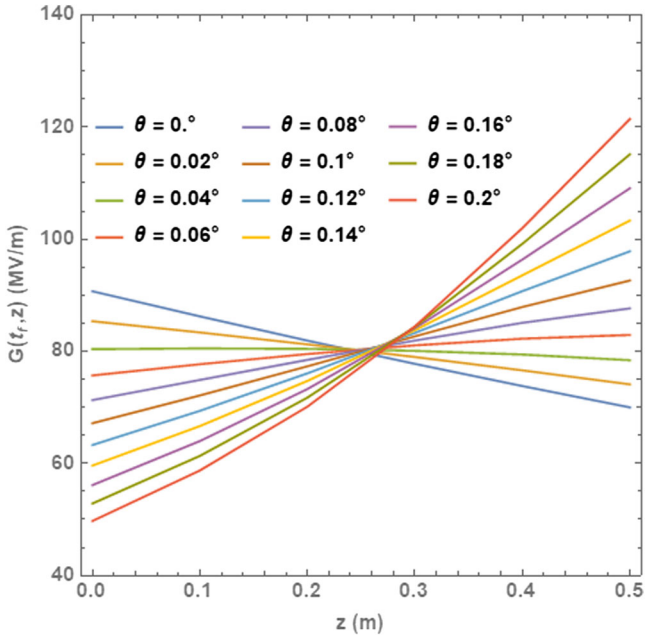

FIG. 12. The accelerating gradient after one filling time as a function of z for $L_s = 0.5$ m for a range of tapering angles θ. The $\sqrt{P_k}$ is chosen such that the average gradient $\langle G \rangle = 80$ MV/m.

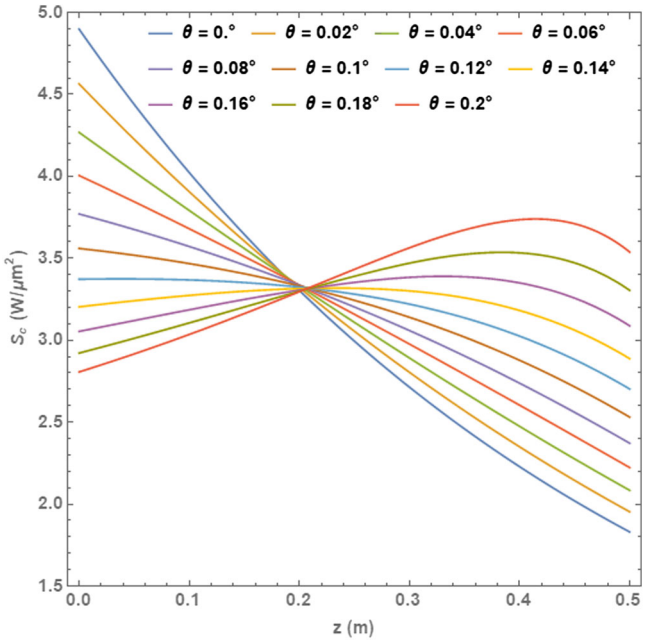

FIG. 13. The modified Poynting vector as a function of z for varying tapering angles θ.

structure lengths are illustrated in Fig. 14. The effective shunt impedance of the structure can be found using the gradient profile [14]:

$$R_s = \frac{1}{L_s P_k}\left(\int_0^{L_s} G_0(t_f - \tau(z))g(z)\mathrm{d}z\right)^2, \qquad (20)$$

where P_k is the input klystron power. By comparing Figs. 14 and 15, it can be seen that increasing the length of the structure increases the effective shunt impedance and therefore the coupling to beam while sacrificing an increase

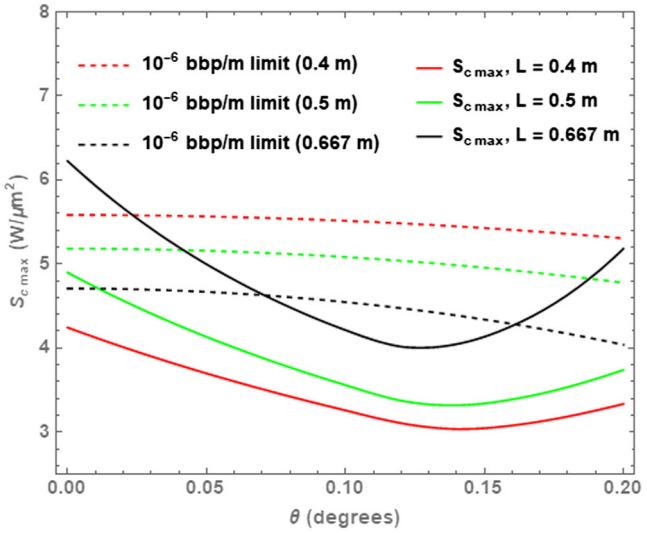

FIG. 14. The peak value of the modified Poynting vector as a function of the tapering angle θ for varying structure lengths.

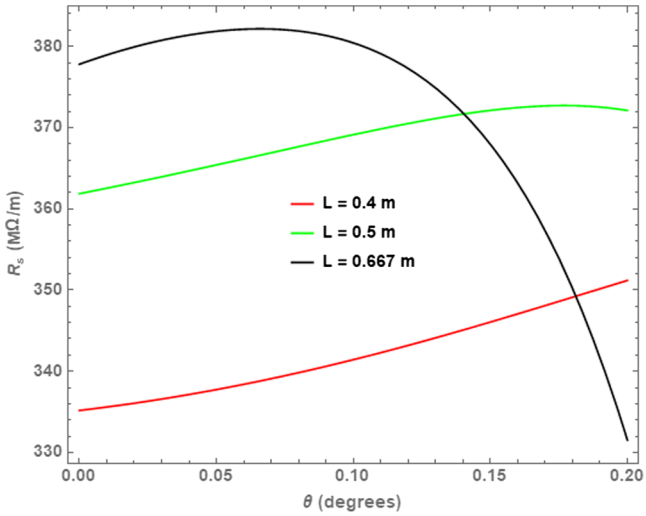

FIG. 15. The effective shunt impedance per unit length for varying structure lengths L_s as a function of tapering angle θ.

in the probability of breakdown. Additionally, a longer structure requires an larger amount of power input as can be seen in Fig. 16. The power is dissipated as it travels through the structure therefore for a longer structure the input power must also be increased to compensate for the dissipated power. Increasing the length of the structure generally increases the amount of rf power needed to accelerate the beam, however fewer structures are required in order to achieve the required energy of the beam. It is possible through the scaling law (19) that if a lower value of S_c is required due to heating effects or requiring a different structure length, it may be achieved through either changing the pulse length of the klystron or by accepting a higher breakdown rate.

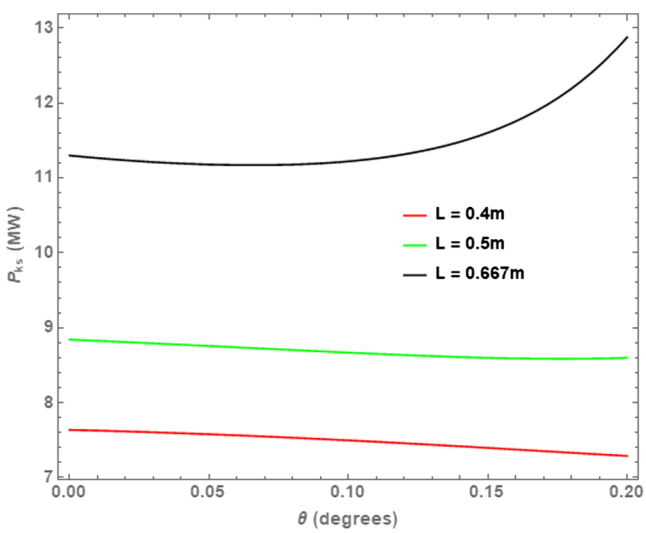

FIG. 16. The power per structure as a function of θ for varying structure lengths.

C. Gaussian taper

While choosing a linear tapering of the linac iris radii may be acceptable in terms of achieving the desired gradient without exceeding the set breakdown limits, dipole bands which have not been detuned may result in large wakefields which degrade the beam quality. To this end, a study to reduce the strength of these wakefields has been carried out by considering a Gaussian taper for a range of standard deviations of the frequency distribution down the linac σ and frequency spread $\Delta\omega$. For a given σ and $\Delta\omega$, the distribution of the dipole frequencies is given by

$$\frac{\mathrm{d}n}{\mathrm{d}\omega} = A\exp\left(-\frac{(\omega-\bar{\omega})^2}{2\sigma^2}\right), \tag{21}$$

$$A = (N-1)\left[\int_{\omega_1}^{\omega_N}\exp\left(-\frac{(\omega-\bar{\omega})^2}{2\sigma^2}\right)\mathrm{d}\omega\right]^{-1}, \tag{22}$$

where A is a normalization constant, N is the number of cells. $\bar{\omega}$ is the average dipole frequency of the structure which is decided by $\langle a\rangle$, and $\omega_1 = \bar{\omega} - \Delta\omega/2$ and $\omega_N = \bar{\omega} + \Delta\omega/2$ are the dipole frequencies of the first and last cells respectively. Once the σ and $\Delta\omega$ are decided, the numerical optimization tool interpolates the rf parameters across the structure similar to the linear tapered case. Note that as the distribution of frequencies is Gaussian, the dipole frequency $\omega(n)/2\pi$ as a function of the cell number n is given as an error function. The reversed relationship is then found and interpolated as shown in Fig. 17.

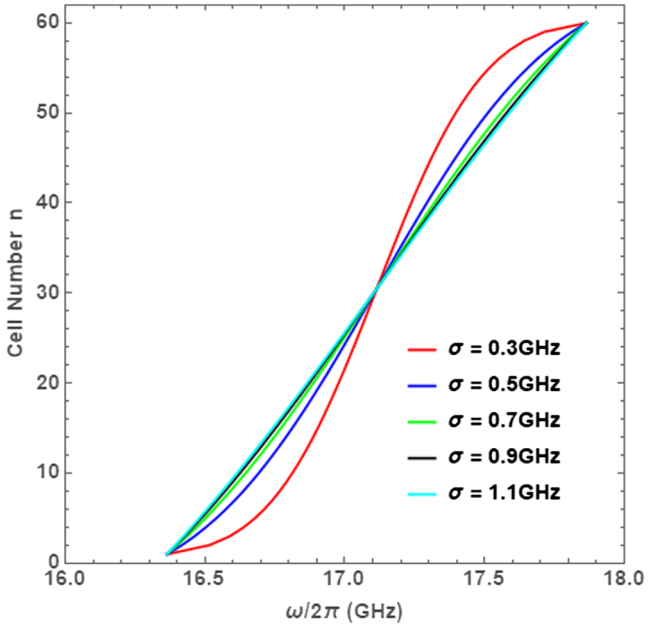

FIG. 17. The dipole frequency $\omega(n)/2\pi$ as a function of the cell number n reversed and interpolated with $L = 0.5$ m and $\Delta\omega/2\pi = 1.5$ GHz.

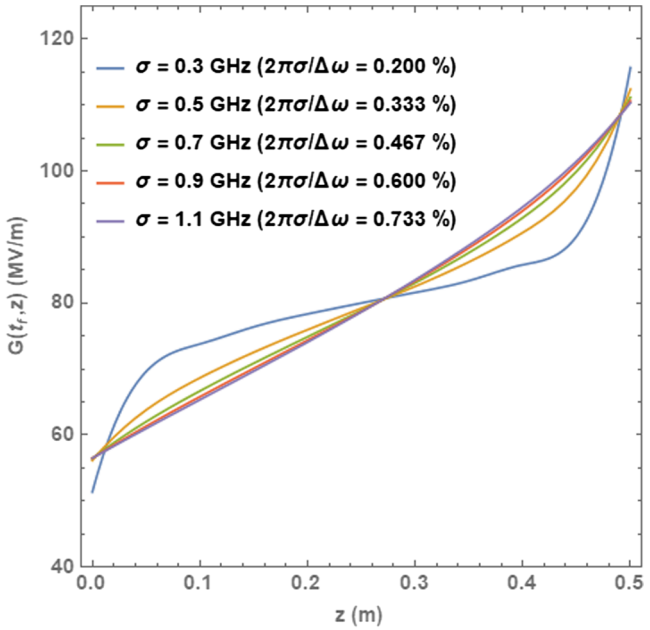

FIG. 18. The gradient profile of a structure with Gaussian tapered irises. The gradient is given for a range of σ where the $\Delta\omega/2\pi = 1.5$ GHz, $L = 0.5$ m and $\langle G\rangle = 80$ MV/m for this example.

Repeating the use of the numerical optimization tool, the gradient, S_{cmax}, R_s, and P_{ks} are calculated for a range of Gaussian structures with $\sigma = [0.3, 1.1]$ GHz and $\Delta\omega/2\pi = [1, 2.5]$ GHz given in Figs. 18–21. Fig 19 shows the maximum modified Poynting vector as a percentage variation from the breakdown limit with values $\Delta S_{cmax} < 0$ being

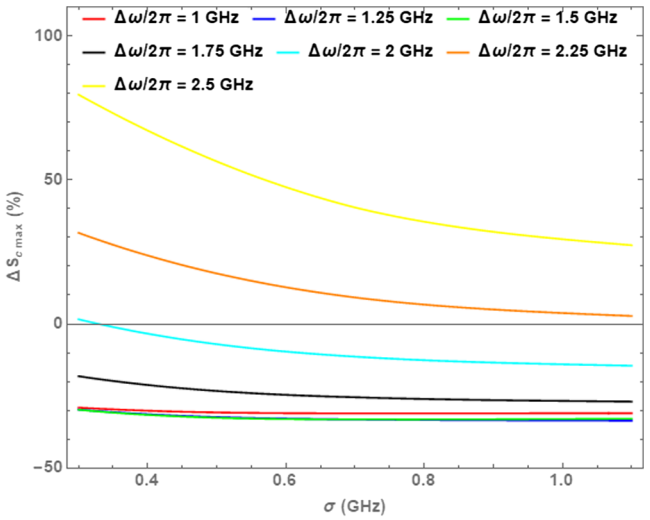

FIG. 19. The percentage variation of the maximum modified Poynting vector over the structure from the breakdown limit described by Eq. (19). A positive value signifies that S_{cmax} exceeds the limit and a negative value is within the limit. ΔS_{cmax} is given for a range of $\Delta\omega$ where $L = 0.5$ m and $\langle G\rangle = 80$ MV/m for this example.

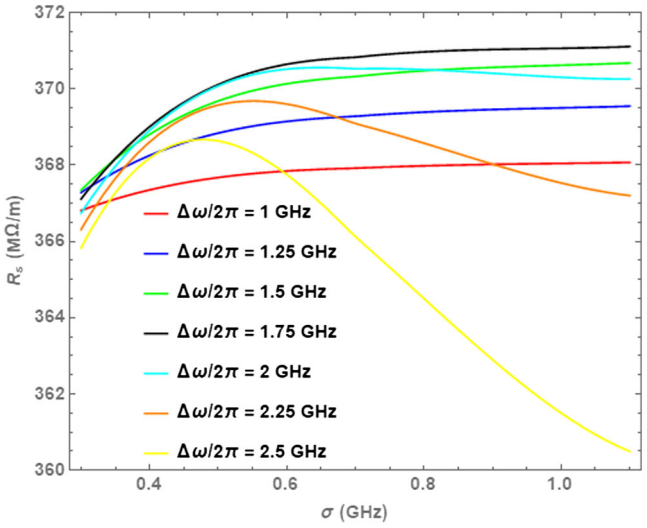

FIG. 20. The effective shunt impedance of the structure as a function of σ for a range of $\Delta\omega$ where $L = 0.5$ m and $\langle G \rangle = 80$ MV/m for this example.

below the allowed breakdown limits. Calculating ΔS_{cmax} yields the allowed values of σ for a given frequency spread $\Delta\omega$.

It can be seen in Fig. 19 that a larger frequency spread leads to a significant increase of breakdown in the structure due to the maximum iris radius in the structure increasing. The structure also becomes less efficient with larger frequency spreads for a given structure length as shown by a reduction in the effective shunt impedance in Fig. 20. This would suggest that in terms of breakdown and rf efficiency a lower frequency spread is beneficial and would be preferred. It can be seen in Fig. 21 that generally the power input required for a Gaussian tapered structure is lower than for a linear tapered structure. However, for a

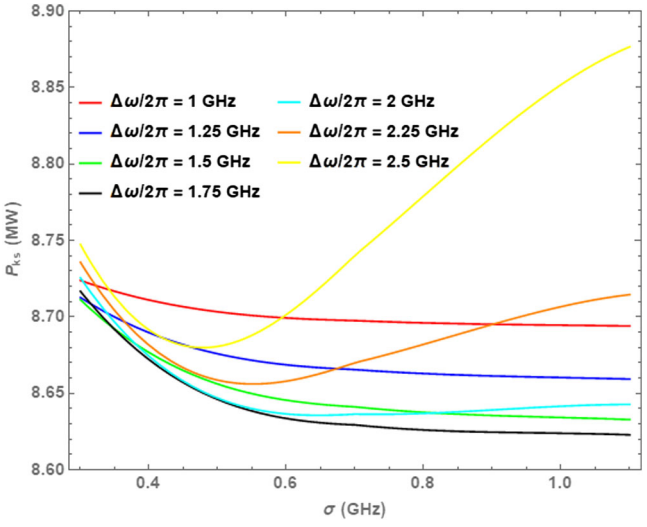

FIG. 21. The klystron power per structure for a range of $\Delta\omega$ where $L = 0.5$ m and $\langle G \rangle = 80$ MV/m for this example.

structure with a larger frequency spread $\Delta\omega$, the iris radii tapering tends toward a linear tapering as σ increases. Therefore, the power input required tends toward that of the linear tapering which can be seen by comparing the curve for $\Delta\omega/2\pi = 2.5$ GHz in Fig. 21 against the curve for $L = 0.5$ m in Fig. 16.

IV. GEOMETRIC WAKEFIELD ANALYSIS

A point particle with charge q that moves parallel to the axis of the linac with offset x and velocity c, will feel a potential $xq_eW(s)$ due to leading particle of charge q_e which is a distance s ahead of the trailing particle. The dipole wakefield is defined by

$$W(s) = 2\sum_n K_n \sin\left(\frac{\omega_n s}{c}\right) \exp\left(-\frac{\omega_n s}{2cQ_n}\right), \quad s > 0, \tag{23}$$

where $K_n, \omega_n/2\pi$ and Q_n are the kick factors, frequencies and quality factors of the nth dipole mode of the structure [23]. It should be noted that there is no explicit dependence on the radial offset r in Eq. (23) as the kick factor defined by Eq. (10) removes the radial offset dependence which originates from the accelerating voltage $V_{acc}(r)$. In this study, the Q values for the structure allow the exponential factor in (23) to be set ≈ 1. For a small distance s behind the leading charge, the wakefield is approximately given by

$$W(s) \approx \int_{-\infty}^{\infty} K(\omega) \frac{\mathrm{d}n}{\mathrm{d}\omega} \sin\left(\frac{\omega s}{c}\right) \mathrm{d}\omega, \tag{24}$$

where $K(\omega)$ is the kick factor as a smooth function of frequency ω. It can be seen that Eq. (24) is given by the (sine) Fourier transform of the quantity $K\mathrm{d}n/\mathrm{d}\omega$. Deciding the distribution of the frequencies in the structure is important as it decides the initial fall-off of the transverse wakefield. The wakefield can be shown to fall off as $W(s) \sim \mathrm{sinc}(\Delta\omega s/c)$ and $W(s) \sim \exp(-2\pi\sigma s/c)^2$ for a linear and Gaussian tapering respectively where $\mathrm{sinc}(x) = \sin(x)/x$.

A. The uncoupled wakefield

In reality, the cells of the linac structure are connected electronically and magnetically through the irises. However, as a first order method the cells are considered to be isolated from each other, i.e., "uncoupled." The uncoupled wakefield of a structure with N cells is given by

$$W_U(s) = \frac{2}{N}\sum_m^N K_s^{(m)} \sin\left(\frac{\omega_s^{(m)} s}{c}\right), \tag{25}$$

where the wake is summed over N cells and $K_s^{(m)}$ and $\omega_s^{(m)}/2\pi$ are the kick factors and frequencies of the dipole mode which is synchronous with the beam for cell m [23]. This takes advantage of the approximation that if the

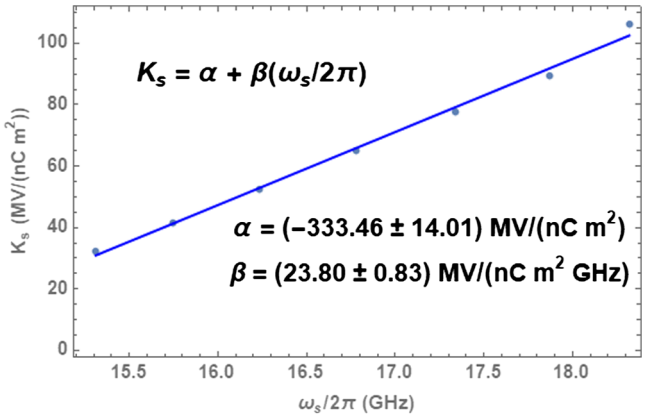

FIG. 22. The dipole kick factors of the single cell as a function of the synchronous frequency of the cell. The dots are values of the kick factors calculated via HFSS for cells A-G of the XARA structure given in Table II. The solid line is a linear fit to the data.

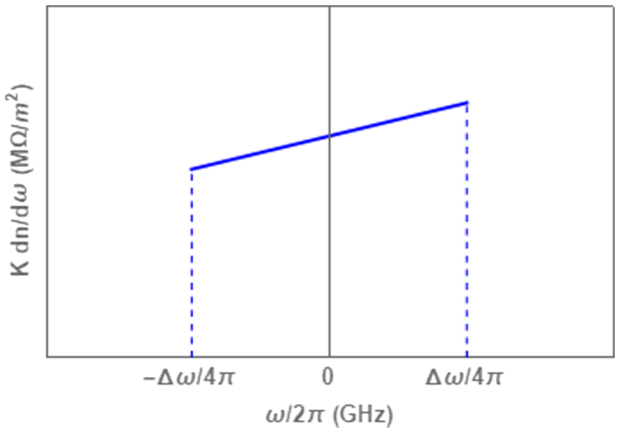

FIG. 23. The profile of the quantity $K\mathrm{d}n/\mathrm{d}\omega$ for a linear tapered structure which is to be Fourier transformed to find the wakefield.

tapering down the structure is gradual and composed of many cells then the wakefield is locally described by the synchronous parameters. The kick factors are generally linear with the synchronous frequency, as shown in Fig. 22.

Knowledge of both the synchronous kick factors and frequencies allow the uncoupled wakefield to be calculated by summation for a given distribution of the irises in the structure. However for larger structures this can require many intermediate calculations to take place to yield the wake. This can be time consuming if a structure is being designed with consideration of minimizing the wakefield. To allow for rapid computation, analytical solutions of the uncoupled wakefield for both linear and Gaussian tapered structures have been derived.

B. Analytical expression

1. Linear taper

The immediate fall-off of the wakefield is given by the Fourier transform of the quantity $K\mathrm{d}n/\mathrm{d}\omega$, i.e. for small s. Therefore, $K\mathrm{d}n/\mathrm{d}\omega$ is recentered around the origin to allow for more straightforward algebra as shown in Fig. 23.

The Fourier transform is then found as

$$\tilde{W}(s) = \int_{-\infty}^{\infty} G(\omega) \exp\left(-\frac{2\pi i \omega s}{c}\right) \mathrm{d}\omega, \tag{26}$$

$$G(\omega) = \begin{cases} m_l\omega + c_l & |\omega| \le \Delta\omega/4\pi \\ 0 & |\omega| \ge \Delta\omega/4\pi \end{cases} \tag{27}$$

where $m_l = [G(\Delta\omega/4\pi) - G(-\Delta\omega/4\pi)]/(\Delta\omega/2\pi)$ is the gradient of $K\mathrm{d}n/\mathrm{d}\omega$ and $c_l = [G(\Delta\omega/4\pi) + G(-\Delta\omega/4\pi)]/2 = G(0)$. Integration by parts and use of exponential identities yields the result

$$\tilde{W}(s) = \frac{c_l \Delta\omega}{2\pi} \mathrm{sinc}\left(\frac{\Delta\omega s}{2c}\right) + i\frac{m_l \Delta\omega c}{4\pi^2 s}\left[\cos\left(\frac{\Delta\omega s}{2c}\right) - \mathrm{sinc}\left(\frac{\Delta\omega s}{2c}\right)\right], \tag{28}$$

where c is the speed of light and $\tilde{W}(s)$ is known as the complex wakefield. The part of the wakefield that the bunch experiences is $\Im\{\tilde{W}(s)\}$. The maximum excursion of the envelope of the wake is given by $\hat{W}_L(s) = |\tilde{W}(s)|$ which can be easier to interpret and gives information about the maximum value of the wakefield. A comparison of the transverse wakefields calculated via the summation method (25) and the analytical expression (28) is illustrated in Fig. 24.

The summation of the kicks of each cell in the $\theta = 0.1$ degrees, $L = 0.5$ m structure are given by $(2/N)\sum_n K_n = \hat{W}(s=0) = 147.51$ MV/(pC m mm) and 149.38 MV/(pC m mm) for the summation and analytical wakes respectively. It should be noted that the wakefields found by the summation and the analytical expression do not

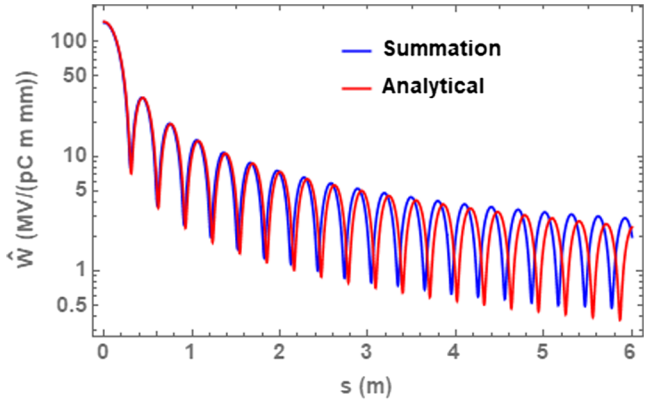

FIG. 24. A comparison of the transverse wakefields calculated via the summation method (25) and the analytical expression (28) for a linear tapered structure of $\theta = 0.1$ degrees and $L = 0.5$ m.

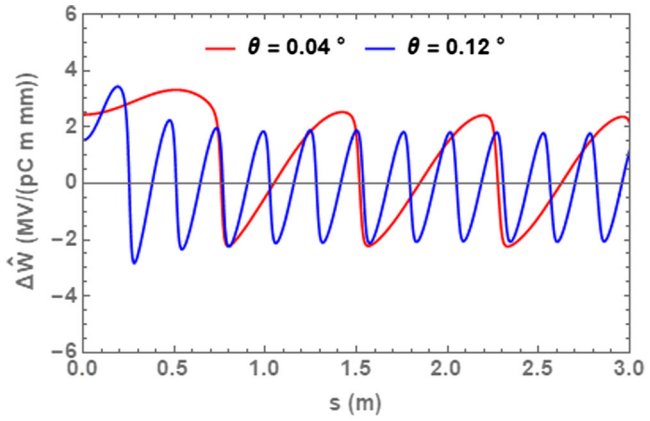

FIG. 25. The difference of the transverse wakefields calculated via the summation method (25) and the analytical expression (28) for $\theta = 0.04$ degrees and $\theta = 0.12$ degrees and $L = 0.5$ m. Note that a restricted list of θ values have been used to make the behavior easier to interpret.

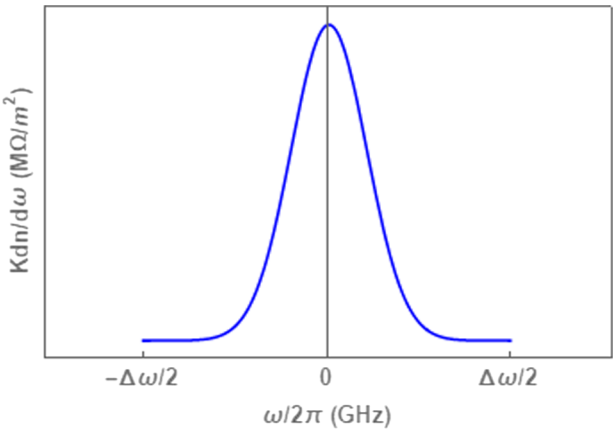

FIG. 26. The profile of the quantity $Kdn/d\omega$ for a Gaussian tapered structure which is to be Fourier transformed to find the wakefield.

yield the exact same result. This is due to the fact that a continuous Fourier transform essentially calculates the wakefield of a infinite structure with a fixed frequency spread. It can be shown that if an artificially large number of points are used in the summation (25), the Fourier Transform will become continuous and tend toward the solution given by the analytical expression. The difference between the two wakes $\Delta\hat{W}(s)$ is shown in Fig. 25 for $\theta = 0.04$ degrees and $\theta = 0.12$ degrees.

While the analytical expression does not yield the exact wakefield, it gives a good representation and has the benefit of being in a closed form and requires fewer calculations allowing for more rapid computation.

2. Gaussian taper

An example of the quantity $Kdn/d\omega$ for a Gaussian taper is shown in Fig. 26.

Again, in order to make this derivation more straightforward, the $Kdn/d\omega$ has be recentered around the origin such that:

$$\frac{dn}{d\omega} = A\exp\left[-\frac{1}{2}\left(\frac{\omega}{\sigma}\right)^2\right], \tag{29}$$

where A is given by Eq. (22). The kick factors are linearly dependent $K(\omega) = m_g\omega/2\pi + c_g/2$ where m_g is the gradient of the linear fit and c_g will be twice the central kick $2K(\omega = \bar{\omega})$ (remembering that the recentred intersect is the central frequency). The problem is then set up as:

$$G(\omega) = \begin{cases} (m_g\omega + c_g/2)A\exp\left(-\omega^2/2\sigma^2\right) & |\omega| \le \Delta\omega/4\pi \\ 0 & |\omega| \ge \Delta\omega/4\pi \end{cases} \tag{30}$$

The Fourier transform is given by:

$$\tilde{W}(s) = \int_{-\infty}^{\infty} G(\omega)\exp\left(-\frac{2\pi i\omega s}{c}\right)d\omega. \tag{31}$$

After some algebra we find that the Fourier transform can be written as

$$\begin{aligned}\tilde{W}(s) = {} & Am_g\exp\left(-\frac{2\sigma^2\pi^2s^2}{c}\right)\left\{\sigma^2\left[-\exp\left(-\frac{1}{2}y_2^2\right)+\exp\left(-\frac{1}{2}y_1^2\right)\right]-\frac{\sqrt{2\pi}\sigma^3\pi is}{c}\left[\mathrm{erf}\left(\frac{y_2}{\sqrt{2}}\right)-\mathrm{erf}\left(\frac{y_1}{\sqrt{2}}\right)\right]\right\} \\ & + A\frac{c_g}{2}\exp\left(-\frac{2\sigma^2\pi^2s^2}{c}\right)\sigma\frac{\sqrt{2\pi}}{2}\left[\mathrm{erf}\left(\frac{y_2}{\sqrt{2}}\right)-\mathrm{erf}\left(\frac{y_1}{\sqrt{2}}\right)\right],\end{aligned} \tag{32}$$

where $y_{1,2} = \frac{1}{\sigma}(\mp\frac{\Delta\omega}{4\pi} + 2\sigma^2\pi is/c)$. However, there needs to be a normalization enforced to satisfy the physical constraint that at $s = 0$, the analytical wake W_g must be given by

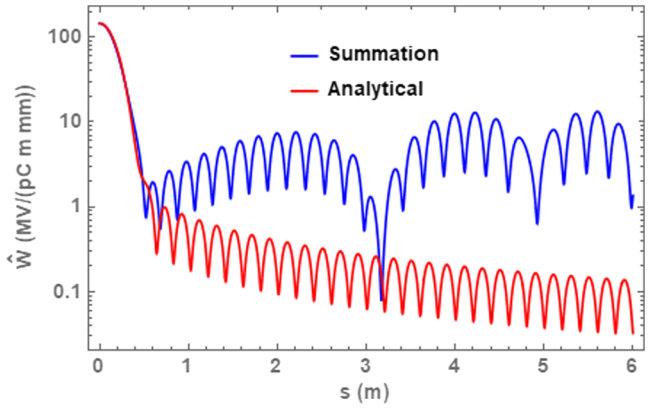

FIG. 27. A comparison of the transverse wakefields calculated via the summation method (25) and the analytical expression (28) for a Gaussian structure of $\sigma = 0.3$ GHz, $\Delta\omega/2\pi = 1.5$ m and $L = 0.5$ m.

$$W_g(0) = \frac{2}{N}\sum_n K_n. \tag{33}$$

It is worth noting that the constant $c_g = 2K(\bar{\omega}) = (2/N)\sum_n K_n$ is twice the average kick over the structure. Therefore, the analytical wake is given by

$$W_g(s) = \frac{2}{N}\sum_n K_n \left|\frac{\tilde{W}(s)}{\tilde{W}(0)}\right| = c_g \left|\frac{\tilde{W}(s)}{\tilde{W}(0)}\right|. \tag{34}$$

The power of the analytical expression given in Eq. (32) is that it is a explicit function of the frequency spread $\Delta\omega$ and the Gaussian standard deviation σ, which allows for the wake to be calculated for a range of $\Delta\omega$ and σ straightforwardly. A comparison of the summation and analytical wakes for a Gaussian structure is shown for $\sigma = 0.3$ GHz, $\Delta\omega/2\pi = 1.5$ GHz and $L = 0.5$ m in Fig. 27, with the difference $\Delta\hat{W}(s)$ given in Fig. 28.

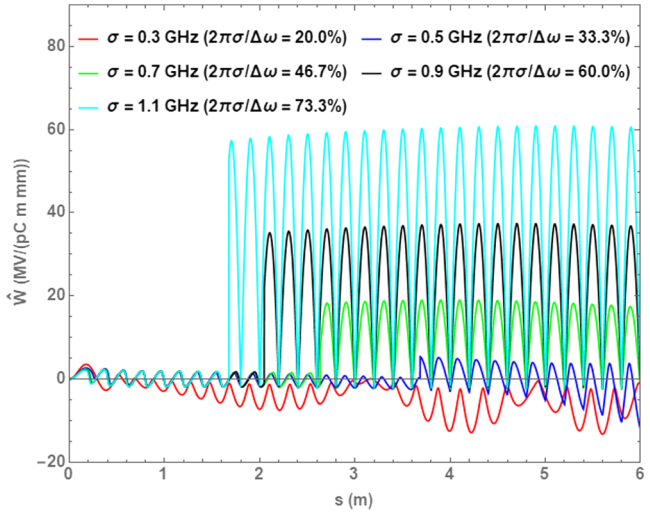

FIG. 28. The difference between the summation method (25) and the analytical expression (28) for a Gaussian structure of fixed $\Delta\omega/2\pi = 1.5$ GHz and $L = 0.5$ m, over a range of σ.

TABLE IV. Optimal overall parameters for the base design of an X-band linac for the XARA upgrade.

Parameter	Value
L_s [m]	0.5
Number of cells	60
σ [GHz]	0.5
$\Delta\omega/2\pi$ [GHz]	1.5
a [mm]	3.88–2.51
Single cell R' [MΩ/m]	92.81–121.32
Q	7101–6989
v_g/c [%]	3.57–0.71
S_{cmax} [A/V]	3.39
Breakdown limit [A/V]	5.02
R_s [MΩ/m]	369.68
P_{ks} [MW]	8.66

It can be shown that for a range of $\Delta\sigma = [0.1, 1.2]$ GHz, $\Delta\omega/2\pi = [0.3, 2.5]$ GHz, the analytical expression agrees well with the summation for small values of s, however the uncoupled wakefield itself is only valid for small values of s. This is due to the coupling between adjacent cells becoming more important as a larger distance behind the leading bunch is considered. In this study, the bunches are far enough apart such that any long-range wakefields excited by the leading bunch are assumed to have dissipated by the arrival of the next bunch. This range of validity allows the initial fall-off of the uncoupled wakefield and short-range behavior to be well described by the analytical structure for both the linear and the Gaussian structures. This is powerful as a design tool as for a required initial falloff, the corresponding tapering angle θ or σ and $\Delta\omega$ can be found straightforwardly and used as a guideline or base design.

For the CLARA multibunch operating scheme, the bunch-to-bunch spacing is 120 ns or 36 m [24] which is outside the range of validity of this study. However in order to future proof this design where shorter bunch spacing may be possible, the wakefield will be investigated for small s. Reviewing Figs. 19–21, a Gaussian structure with $\sigma = 0.5$ GHz and $\Delta\omega/2\pi = 1.5$ GHz for a length of $L = 0.5$ m gives a good compromise between the rf efficiency, the breakdown limit and the initial fall off of the geometric transverse wakefield. The parameters for this optimal structure are given in Table IV.

V. SHORT-RANGE TRANSVERSE WAKEFIELDS

A. The point-charge wakefield

The long-range transverse wakefields will only become significantly problematic if multibunch operation of XARA is used. However, initially only a single-bunch regime will be utilized and therefore, knowledge of the short-range

wakefield is critical for the XARA design process. In reality, structure misalignments or orbit errors in the linac will produce a growth in the projected emittance of the beam due to the short-range wakefields and degrade the quality of the beam. For an electron bunch with longitudinal distribution λ at longitudinal position s, the transverse kick is given by

$$V_x(s) = q\int_{-\infty}^{s} W_x(s-s')x(s')\lambda(s')\mathrm{d}s', \tag{35}$$

where q is the charge of the bunch and x is the transverse offset of the bunch [25]. The normalized kick along the bunch, i.e., the bunch wake is

$$\mathcal{W}_x(s) = q\int_{-\infty}^{s} W_x(s-s')\lambda(s')\mathrm{d}s', \tag{36}$$

and the average kick over the entire bunch (the total bunch kick factor) is given by

$$\mathcal{K}_x(s) = \int_{-\infty}^{\infty} \mathcal{W}_x(s)\lambda(s)\mathrm{d}s. \tag{37}$$

For a perfectly conducting disk-loaded structure with geometry given in Fig. 29, the high frequency longitudinal impedance for large k is given by [26]

$$Z_L(k) = \frac{iZ_0}{\pi k a^2}\left[1 + (1+i)\frac{\alpha(\eta = g/L)L}{a}\sqrt{\frac{\pi}{kg}}\right]^{-1}, \tag{38}$$

where k is the wave number, $Z_0 = 120\pi\,\Omega$ and $\alpha(\eta)$ can be approximated by

$$\alpha(\eta) \approx 1 - \alpha_1\sqrt{\eta} - (1-2\alpha_1)\eta, \tag{39}$$

where $\alpha_1 = 0.4648$. The inverse Fourier transform of the longitudinal impedance yields the short-range longitudinal wakefield for small s:

$$W_L(s) \approx \frac{Z_0 c}{\pi a^2}\phi(s)\exp\left(\frac{\pi s}{4s_{00}}\right)\mathrm{erfc}\left(\frac{\pi s}{4s_{00}}\right), \tag{40}$$

where $\phi(s)$ is the step function, $\mathrm{erfc}(x)$ is the complex error function and

$$s_{00} = \frac{g}{8}\left(\frac{a}{\alpha(g/L)L}\right)^2. \tag{41}$$

The short-range longitudinal wake can be written in a simpler form while retaining the leading order dependence on s that is consistent with Eq. (38). The transverse short-range wakefield can then be found as [26]

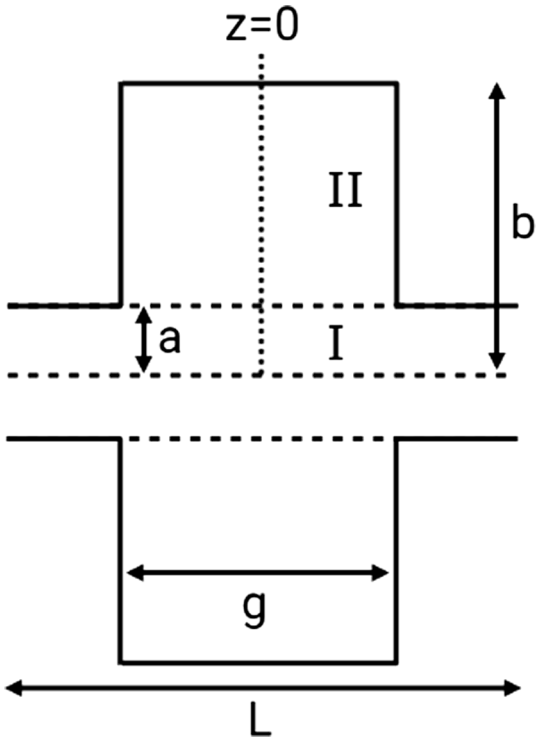

FIG. 29. The cell geometry used to calculate the short-range transverse wakefield where all parameters have their usual meanings. Region I is the beam pipe of the structure and region II is the cell cavity for $a < r < b$ and $-L/2 < z < L/2$.

$$W_x = \frac{2}{a^2}\int_0^s W_L(s')\mathrm{d}s', \tag{42}$$

$$W_x(s) = \frac{4Z_0 c s_{00}}{\pi a^4}\phi(s) \times\left[1 - \left(1 + \sqrt{\frac{s}{s_{00}}}\right)\exp\left(-\sqrt{\frac{s}{s_{00}}}\right)\right]. \tag{43}$$

The short-range dipole wakefield can be calculated using a computer code developed by K. Yokoya [27] which is based on an impedance field matching technique by H. Henke [28] and referred to as the complex frequency domain (CFD) code in this paper. This code calculates the impedance of a periodic structure shown in Fig. 29 with the cell radii $b \to \infty$ by field matching. In contrast to other codes, this program finds the impedance along a contour in the complex plane which is shifted by an amount $\mathrm{Im}(k)$ above the real axis instead of along the real axis itself. When the real k axis is used, the real part of the impedance R_x is given by a sum of delta functions which results in a spiky function. Similarly, the imaginary part of the impedance X_x becomes a quickly varying function along the real k axis. However when a contour in the complex plane is used, both the real and imaginary components become smoother functions of the frequency which are easier to numerically Fourier transform via computer codes.

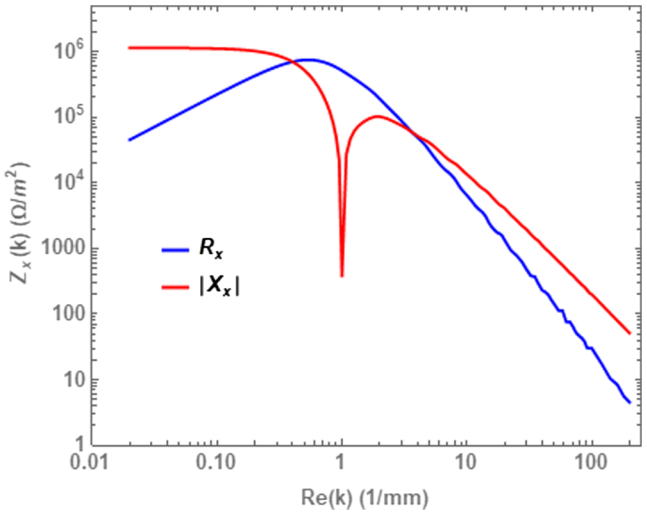

FIG. 30. The real R_x and absolute value of the imaginary $|X_x|$ parts of the transverse impedance of the mid cell of the XARA structure as calculated by the numerical CFD code for $\mathrm{Im}(k) = 0.5\ \mathrm{mm}^{-1}$.

A disadvantage of this method, however, is that the inverse Fourier transform yields a wakefield in the form $\exp(\mathrm{Im}(k)s)F(s)$ where for large s the function $F(s)$ becomes very small and no longer accurately represents the short-range wakefield. This limits the range of s that can practically be computed for a given value of $\mathrm{Im}(k)$.

To demonstrate the results of the CFD code, the real and imaginary parts of the impedance for the mid cell of the XARA structure with $a = 3.208$ mm, $b = 10.456$ mm, $g = 6.332$ mm and $L = 8.332$ mm are shown in Fig. 30.

The transverse wakefield W_x can be found by the inverse Fourier transform of the impedance via

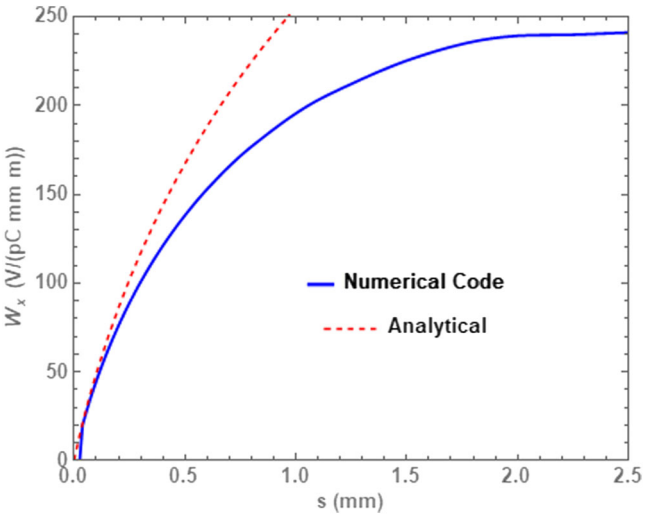

FIG. 31. The transverse short-range wakefield calculated from the impedances shown in Fig. 30 of the mid cell of the XARA structure (solid). Also shown is the analytical short-range wakefield as calculated by Eq. (43) (dashed).

$$W_x(s) = \frac{2c}{\pi}\int_0^\infty R_x(k)\sin(ks)\mathrm{d}k, \tag{44}$$

which is analytically independent of the value chosen for $\mathrm{Im}(k)$. Eq. (44) can also be written in terms of the imaginary part of the impedance X_x by use of the Kramers-Kronig relation, both of which are calculated in the impedance code to ensure accuracy and consistency. The transverse short-range wakefield of the XARA mid cell has been calculated from the both R_x and $|X_x|$ in Fig. 30 and is given in Fig. 31.

Also shown in Fig. 31 is the analytical short-range wakefield as calculated by Eq. (43) which approximates the numerical result well near the origin and up to a range of ~0.2 mm. However in order to produce the behavior of the wakefield for a large number of cells, it becomes useful to create a fitted wakefield function which is accurate over a valid range of geometrical parameters. First, the impedance code is used to calculate the wakefield results for cells within a parameter range $0.34 \le a/L \le 0.69$ and $0.54 \le g/L \le 0.89$. These results are then used to find a fitted function of the same form as the asymptotic, short-range solution [25]:

$$W_x(s) = \frac{4Z_0 c s_0}{\pi a^4}\phi(s) \times \left[1 - \left(1 + \sqrt{\frac{s}{s_0}}\right)\exp\left(-\sqrt{\frac{s}{s_0}}\right)\right], \tag{45}$$

where the new fitting parameter is given as

$$s_0 = \mu\frac{a^\beta g^\gamma}{L^\delta}, \tag{46}$$

where μ, β, γ, δ are parameters to be found. Results of the CFD code for the cell parameter range and Eq. (46) with $\mu = 0.169$, $\beta = 1.80$, $\gamma = 0.3335$, $\delta = 1.13$ are shown in Fig. 32. It can be seen by this fit that the transverse short-range wakefield is strongly dependant on the iris size a but weakly dependant on the cell gap g, causing a larger wakefield as the iris size reduces as expected. This also suggests that the wakes can be modified with changes to the cell gap but would only be useful for fine tuning due to the weak dependence.

The fitted parameter s_0 can be seen in Fig. 32 to agree better with results for cells with smaller values of a/L suggesting that values $a/L \ge 0.69$ may be outside of the range of validity of this study. This limitation may be explained by noting that the analytical form of the short-range wakefield is valid for high frequency where higher order terms have been neglected [25]. It can also be noted that the values of μ, β, γ, δ can be altered to force agreement between the numerical results and the fitted results for a different range of g/L and may be more useful depending on which value of g/L is being used in the cell design.

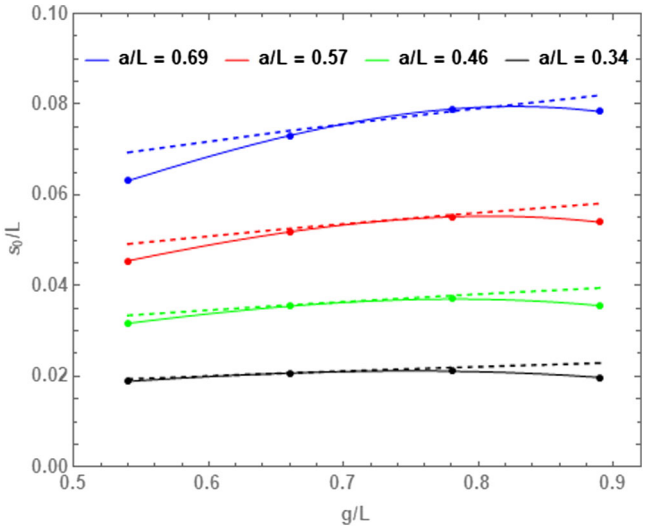

FIG. 32. Results of a parameter study to calculate s_0 for the transverse wake by use of the CFD code for 16 points (dots) chosen with in the ranges $0.34 \leq a/L \leq 0.69$ and $0.54 \leq g/L \leq 0.89$. Interpolation of these points are shown by a solid line. A fit of Eq. (46) with $\mu = 0.169$, $\beta = 1.80$, $\gamma = 0.3335$, and $\delta = 1.13$ are shown by dashed lines.

The fitted value of s_0 can be used in Eq. (45) to yield the wakefield for the valid ranges of a/L and g/L that have been considered. Comparisons of these fitted wakes and wakes calculated via the CFD code are given in Fig. 33 for $a/L = 0.69, 0.57, 0.46, 0.34$.

This has been repeated to observe the comparisons between the CFD code and the fitted wakefields for cells 1, 15, 25, 30, 35, 45 and 60 of a Gaussian tapered structure with $L = 0.5$ mm, $\sigma = 0.5$ GHz and $\Delta f = 1.5$ GHz,

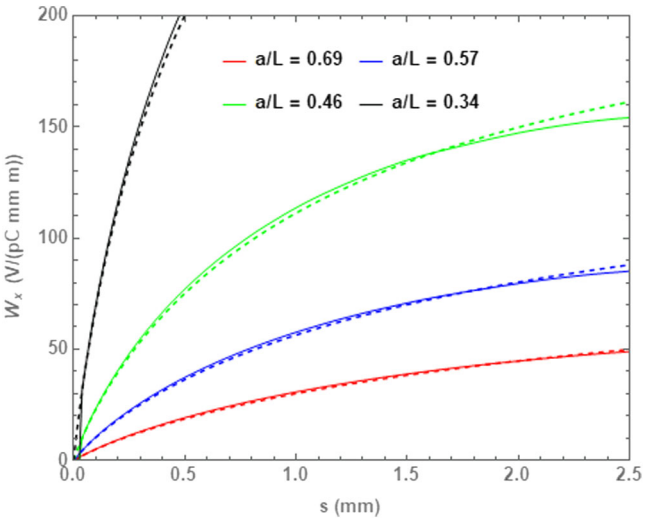

FIG. 33. The short-range wakes calculated via the CFD code (solid) and the fitted wakes (dashed) found by Eq. (45). The two methods of yielding the wakes agree well over the considered range of a/L.

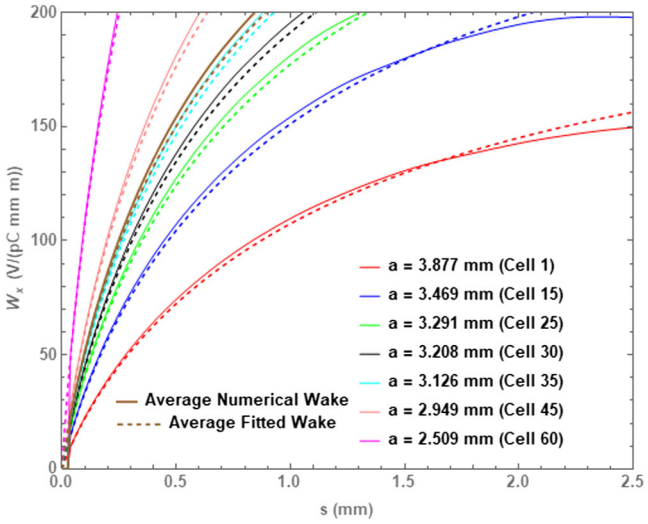

FIG. 34. The short-range wakes for representative cells 1, 15, 25, 30, 35, 45 and 60 of a Gaussian tapered structure with $L = 0.5$ mm, $\sigma = 0.5$ GHz and $\Delta\omega/2\pi = 1.5$ GHz calculated via the CFD code (solid) and the fitted wakes (dashed) found by Eq. (45). The average wakes are also given.

shown in Fig. 34 respectively. Plotting a comparison between the numerical results and analytical formulation allows a solid justification that the analytical fit of the short-range transverse wakes is valid over the range of geometrical parameters considered for the XARA cells. It is also important that the analytical wake is accurate up to a large enough distance s behind the leading bunch. This will allow any bunch length considered for the XARA structure to be convoluted with the wakefield without concerns about errors stemming from the analytical fit.

In Fig. 34, the averaged values of the numerical wakes and fitted wakes across the representative cells are also plotted. To a good approximation, for the short-range wake the averaged wake of the individual cells gives a good representation of the wake of the whole structure. For this structure, the averaged wake is approximately equal to the wake of cell 35. However, for short structures where it is found that the averaged wake does not accurately represent the structure, a more sophisticated model of the short-range wakefields is required [29]. For this study, it is assumed that the averaged wake represents the structure to a reasonable degree.

B. The bunch wakefield

The bunch wakefield has been calculated using the simulation codes ABCI [30] and ECHO2D [31]. These programs employ finite difference techniques to solve Maxwell's equations for a given geometry, returning the wakefield for a given bunch traveling through the structure. The transverse bunch wakefield $\tilde{W}_x$ is found from the point-charge wakefield via [14]

$$\tilde{W}_x = \frac{1}{Q_b}\int_0^\infty W_x(s')\lambda(s-s')\mathrm{d}s', \tag{47}$$

where Q_b is the bunch charge, W_x is the transverse point-charge wakefield and λ is the longitudinal charge distribution of the bunch which is taken to be Gaussian:

$$\lambda(s) = \frac{1}{\sqrt{2\pi}\sigma_z}\exp\left(-\frac{s^2}{2\sigma_z^2}\right), \tag{48}$$

with σ_z the standard deviation of the bunch length. Currently the CLARA Phase 2 machine is planned to act as the S-band injector for XARA and provide a ~250 pC, sub-ps FWHM electron bunch for the XARA linac [2]. For a 1 ps FWHM bunch, the standard deviation is given by $\sigma_z = 0.127$ mm, therefore $\sigma_z = 0.1$ mm is considered for calculations of the bunch wakefields in this paper. The transverse bunch wakes with $\sigma_z = 0.1$ mm for cells A-G of the XARA design, as given in Table II, are shown in Fig. 35 where the head and tail of the bunch is given at $s = -0.4$ mm and $s = 0.4$ mm respectively.

To benchmark these results, simulations have been carried out using the wakefield codes ACBI and ECHO2D to calculate the bunch wake of Cell D of the XARA design with $\sigma_z = 0.1$ mm. Simulations were repeated with increasing fine mesh until the results were shown to not improve significantly when compared to the amount of CPU time used to yield the result. It is worth noticing that the impedance code used to produce the point-charge wakes utilizes a field-matching technique [28] which models the structure as infinitely periodic and then calculates the short-range wake for the whole structure which is then divided by the number of cells used. In order to reproduce these results in ABCI and ECHO2D, an increasing number of identical cells were modeled until the accuracy of the results were shown to no longer be computationally efficient. The short-range wake per cell was calculated and comparisons between the impedance code, ABCI and ECHO2D are shown in Fig. 36.

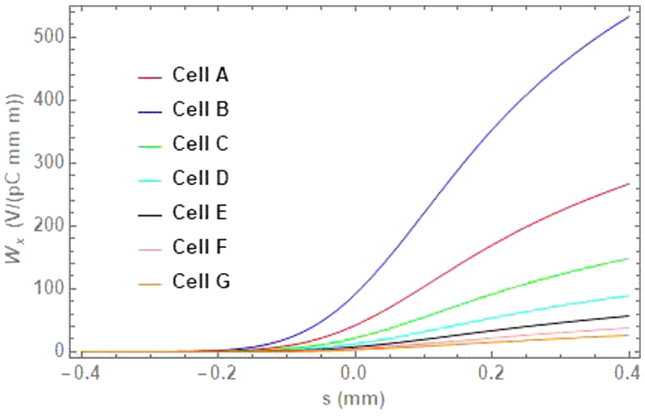

FIG. 35. The short-range transverse bunch wakes for cells A-G of the XARA design, as given in Table II, for a electron bunch with $\sigma_z = 0.1$ mm. The bunch wakefields were calculated using the analytical fit of the transverse wakefields given by Eq. (45). It can be seen that for decreasing iris radii, the transverse wakes become stronger.

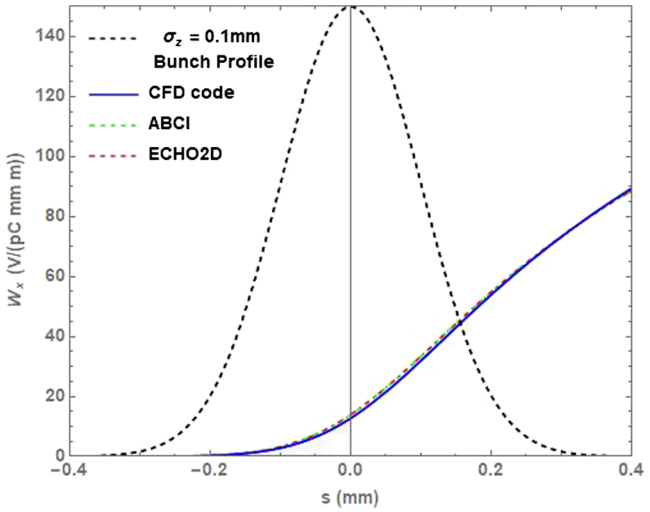

FIG. 36. A comparison of the short-range transverse bunch wake for cell D of the XARA design as calculated by the Complex Frequency Domain code (CFD) (solid blue), ABCI (dashed green) and ECHO2D (dashed red). The Gaussian bunch profile in arbitrary units is also shown (dashed, black).

The results obtained from the CFD code, ABCI and ECHO agree well with each other and with the CFD method taking a factor of ≈20–30 less CPU time compared to the other codes.

VI. SHORT-RANGE LONGITUDINAL WAKEFIELDS

A. The point-charge wakefield

The real and imaginary parts of longitudinal impedance R_L and X_L for the mid-cell of the XARA design as found by the CFD code is shown in Fig. 37 for $\mathrm{Im}(k) = 0.5$ mm^{-1}.

Following from the inverse Fourier transform of the longitudinal impedance given in Eq. (40), the short-range wake can be written more simply with the leading order of s consistent with (38) up to the $\sqrt{s}$ term:

$$W_L(s) \approx \frac{Z_0 c}{\pi a^2}\phi(s)\exp\left(-\sqrt{\frac{s}{s_{00}}}\right). \tag{49}$$

Similar to the short-range transverse wake, a parameter study can also be carried out for the longitudinal wake to produce an analytical expression useful for design purposes. Anticipating the analytical form

$$W_L(s) = \frac{Z_0 c}{\pi a^2}\phi(s)\exp\left(-\sqrt{\frac{s}{s_0}}\right), \tag{50}$$

a fit to the wake is found where s_0 has the same form as Eq. (46) but the exponents are now different. Again, wakes

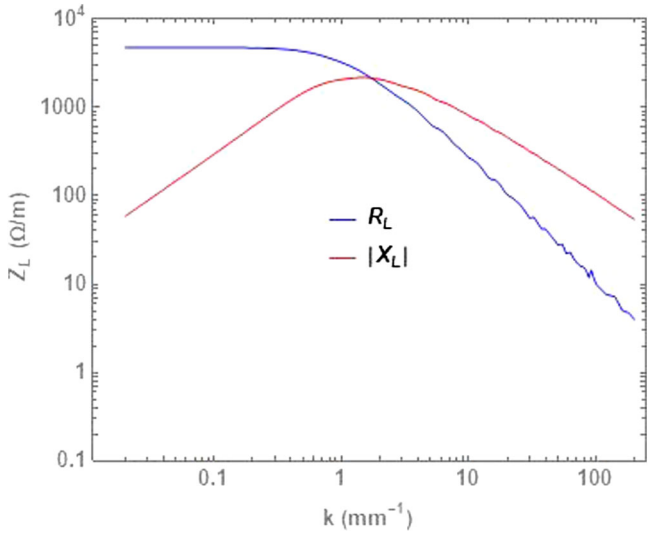

FIG. 37. The real R_x and absolute value of the imaginary $|X_x|$ parts of the longitudinal impedance of the mid cell of the XARA structure as calculated by the CFD code for $\mathrm{Im}(k) = 0.5$ mm^{-1}.

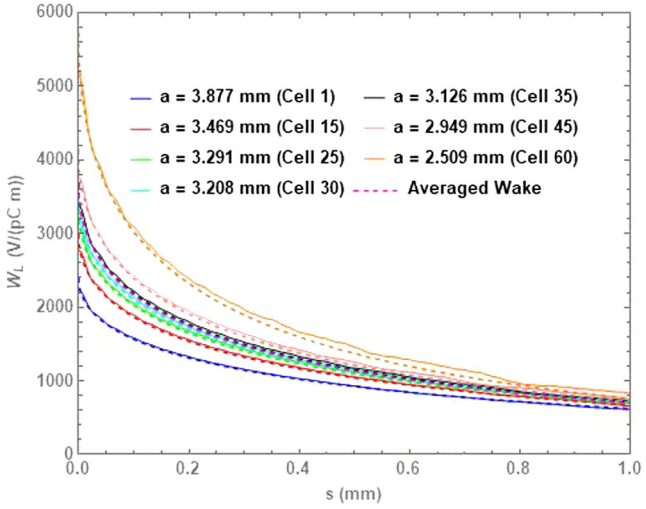

FIG. 39. The longitudinal short-range wakes for the representative cells (cells 1, 15, 25, 30, 35, 45, and 60) are calculated via the CFD code (solid) and the fitted wakes (dashed) found by Eq. (50). Also shown is the average of the fitted wakes of the cells which approximately represents the full structure.

were calculated in the ranges $0.34 \leq a/L \leq 0.69$ and $0.54 \leq g/L \leq 0.89$ and fits were made to determine the vales of μ, β, γ and δ. The results of these fits over the given ranges are shown in Fig. 38 with $\mu = 0.250, \beta = 1.86, \gamma = 1.75$ and $\delta = 2.73$ which have been chosen such that the fits are more suited to the values of a/L and g/L for that of the XARA design.

For the XARA structure, the iris radius of the mid cell is $a = 3.208$ mm giving values of $a/L = 0.385$ and $g/L = 0.760$. It can be seen that the selection of the parameter exponents have been prioritized to return a fit which agrees well with the CFD code for these values of a/L and g/L. However if the values of a or g need to be changed in further designs, these fits are still valid and useful. A comparison of the wakes found by the fits and the results of the CFD code are given in Fig. 39 for the representative cells of the XARA design.

It can be seen that the CFD code can return noisy results for smaller iris radii, however this can be resolved by using the fitted wake due to it being a smooth function.

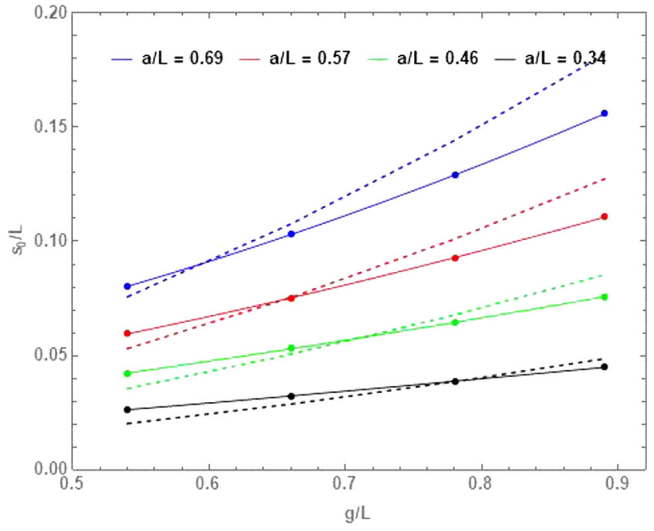

FIG. 38. Results of a parameter study to calculate s_0 for the longitudinal wake by use of the CFD code for 16 points (dots) chosen with in the ranges $0.34 \leq a/L \leq 0.69$ and $0.54 \leq g/L \leq 0.89$. Interpolation of these points are shown by a solid line. A fit of Eq. (46) with $\mu = 0.250, \beta = 1.86, \gamma = 1.75$ and $\delta = 2.73$ are shown by dashed lines.

B. The bunch wakefield

The short-range longitudinal bunch wakefield $\tilde{W}_L$ can be calculated from the point-charge wake W_L via

$$\tilde{W}_L = -\int_0^\infty W_L(s')\lambda(s-s')\mathrm{d}s'. \tag{51}$$

The short-range longitudinal bunch wakefields for cells A-G with a bunch of $\sigma_z = 0.1$ mm are given in Fig. 40.

As with the transverse bunch wakes, the longitudinal bunch wakes have been obtained using ABCI and ECHO2D where similar limitations regarding meshing and number of cells used apply. A comparison of the longitudinal wakes of cell D found by the CFD code, ABCI, and ECHO2D is given in Fig. 41.

A discrepancy arises when calculating the longitudinal wake for cell D via ABCI when compared to the other two methods. This is mostly likely due to the fact that ABCI uses a fixed meshing scheme where the entire structure is meshed before calculations take place. When a large amount of cells is used to replicate the conditions of the field-matching technique of the CFD code, the aspect ratio

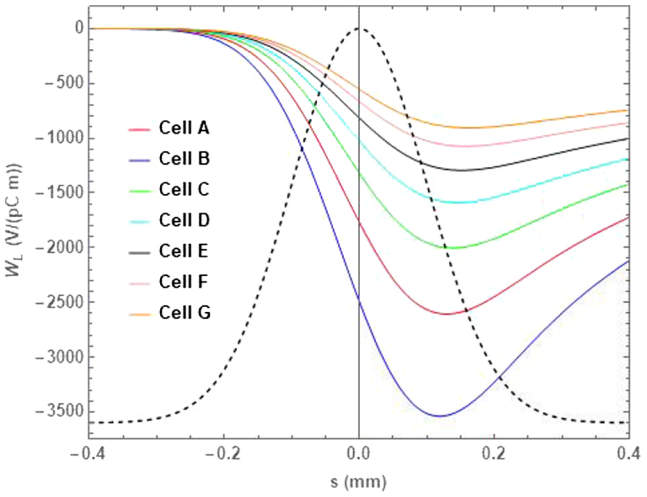

FIG. 40. The short-range longitudinal bunch wakes for cells A-G of the XARA design for a electron bunch with $\sigma_z = 0.1$ mm. It can be seen that for decreasing iris radii, the longitudinal wakes become stronger. The dashed black line shows the longitudinal bunch profile in arbitrary units.

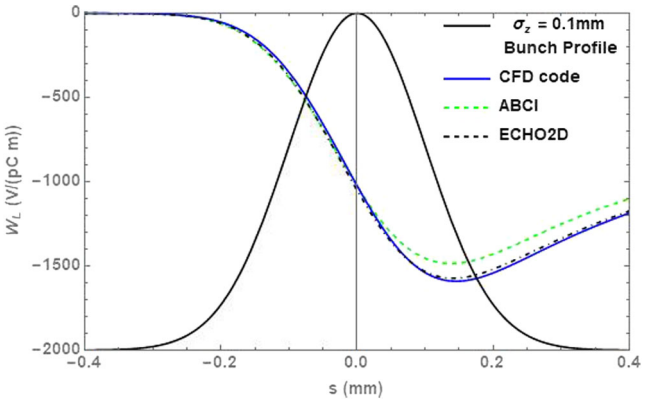

FIG. 41. A comparison of the short-range longitudinal bunch wake for cell D of the XARA design as calculated by the CFD code (solid blue), ABCI (dashed green) and ECHO2D (dashed black). The Gaussian bunch profile in arbitrary units is also shown (solid black).

is stretched and it becomes more difficult to capture small changes in geometry accurately. Due to ECHO2D using a moving mesh frame that travels alongside the beam position, this phenomenon does not arise in ECHO2D and obtains a more accurate wake. It is possible to reduce the discrepancy between the codes, however this was not deemed efficient in terms of computational time.

VII. BEAM DYNAMICS SIMULATIONS

To assess the effects of the short-range wakefields of the initial XARA design on a $\sigma_z = 0.1$ mm electron bunch, the average wakes were calculated to represent the structure. These averaged wakes were then used in the beam dynamics code ELEGANT to calculate how the beam quality changes when traversing through the XARA X-band linac. As the CLARA Phase 2 machine which is planned to be used as an injector to the XARA upgrade is not yet complete, the exact parameters of the beam that will enter the linac are not known. For the purposes of this study, initial beam parameters are estimated to be values which are considered realistic but conservative. The initial beam parameters are given in Table V. Both the emittance and the centroid position of the bunch as it travels through the linac are important quantities to have knowledge of as they give information about how the quality of the beam evolves. In extreme cases, the wakefields can disrupt the beam to an extent where the beam can be kicked into the walls of the structure and beam break up (BBU) occurs where the beam is lost altogether [32]. However for the XARA system the main mode of operation is single-bunch and therefore short-range wakefields that dilute the emittance of the bunch are of importance and it is assumed that wakes dissipate in the time between bunches.

One concern of the XARA structure is its limitations in terms of how much charge can be placed into a single bunch before wakefield effects become significant. To explore this issue, multiple ELEGANT runs have been carried out with increasing bunch charge $Q = 0.25$, 0.5 and 1 nC.

Additionally any misalignment in the structure or initial offset in the bunch will give rise to wakefields that will displace the beam transversely. To represent these effects, initial offsets of the beam of $C_x = \sigma_x/2$ and σ_x have been chosen to see the effects on the beam position further downstream. We also normalize the phase space coordinates to dimensionless coordinates $(X, X') = (x/\sqrt{\beta_x \epsilon_x}, (\alpha_x x + \beta_x x')/\sqrt{\epsilon_x \beta_x})$ where x is the horizontal offset of the bunch, $x' = \mathrm{d}x/\mathrm{d}z$ is the angular divergence of the beam, ϵ_x is the horizontal emittance of the bunch, α_x is the horizontal Twiss alpha function and β_x is the horizontal Twiss beta function [33]. The normalized emittance ϵ_n is found from the

TABLE V. Initial beam parameters used for ELEGANT simulations of the XARA design structure.

Parameter	Value
Central momentum p_0 [MeV/c]	180
Bunch charge Q_b [nC]	0.25, 0.5, 1
Twiss horizontal beta function β_x [m]	25
Twiss vertical beta function β_y [m]	25
Twiss horizontal alpha function α_x	0
Twiss vertical alpha function α_y	0
Macroparticles per bunch	10000
Electron bunch standard deviation σ_z [mm]	0.1
Normalized RMS horizontal emittance ϵ_{nx} [m-rad]	5×10^{-6}
Normalized RMS vertical emittance ϵ_{ny} [m-rad]	0.4×10^{-6}
$\sigma_x = \sqrt{\beta_x \epsilon_x}$ [mm]	0.506
$\sigma_y = \sqrt{\beta_y \epsilon_y}$ [mm]	0.143
Horizontal centroid position C_x	$\sigma_x/2, \sigma_x$

emittance as $\epsilon_n = \beta_z \gamma_L \epsilon$ where $\beta_z = v/c$ with v the beam velocity and γ_L is the relativistic Lorentz factor. This normalization of the phase space allows a unit circle to be marked out in the phase space which represents the σ_x of the initial beam, i.e., the RMS width of the beam. The transformation to the coordinates (X, X') also transform the ellipse in the (x, x') phase space, which represents the emittance, to a unit circle. Circles representing $3\sigma_x$ and $5\sigma_x$ are also marked out so it can be seen more clearly how the profile of the beam changes in phase space. The Twiss parameters α, β, γ of the final beam state after passing through the full structure can be directly calculated via phase space statistics:

$$\begin{aligned}
\epsilon_x &= \sqrt{\langle x^2 \rangle \langle x'^2 \rangle - \langle x x' \rangle}, \\
\alpha_x &= -\frac{\langle x x' \rangle}{\epsilon_x}, \\
\beta_x &= \frac{\langle x^2 \rangle}{\epsilon_x}, \\
\gamma_x &= \frac{\langle x'^2 \rangle}{\epsilon_x},
\end{aligned} \tag{52}$$

where the moments of the phase space distribution are given by

$$\begin{aligned}
\langle x \rangle &= \frac{1}{N} \sum_{i=1}^{N} x_i, \\
\langle x' \rangle &= \frac{1}{N} \sum_{i=1}^{N} x'_i, \\
\langle x^2 \rangle &= \frac{1}{N} \sum_{i=1}^{N} (x_i - \langle x \rangle)^2, \\
\langle x'^2 \rangle &= \frac{1}{N} \sum_{i=1}^{N} (x'_i - \langle x' \rangle)^2, \\
\langle x x' \rangle &= \frac{1}{N} \sum_{i=1}^{N} (x_i - \langle x \rangle)(x'_i - \langle x' \rangle),
\end{aligned} \tag{53}$$

where N is the number of particles used and parameters with subscript i are values of the ith particle. The Twiss parameters given in Eq. (52) have been calculated manually from the final phase space and have been compared to those output by ELEGANT to good agreement.

The X-band linac section of XARA will comprise 3 or 4 modules consisting of a high-power rf source of one or two 50 MW X-band klystrons, a low loss waveguide and a SLED pulse compressor which feed into the X-band structure. Assuming the use of 3 modules with 8 rf structures each for a total of 24 structures, ELEGANT simulations have been done to assess the beam quality as it travels through the entire XARA system. Currently, only the transverse wakes have been included in the ELEGANT simulations. Longitudinal effects on the beam caused by the longitudinal wakes are under investigation and will be presented in future works. The normalized phase space plots for the 24 cavity structure for beam charge values $Q_b = 0.25$, 0.5 and 1 nC for beam offsets of $C_x = \sigma_x/2, \sigma_x$ are given in Fig. 42.

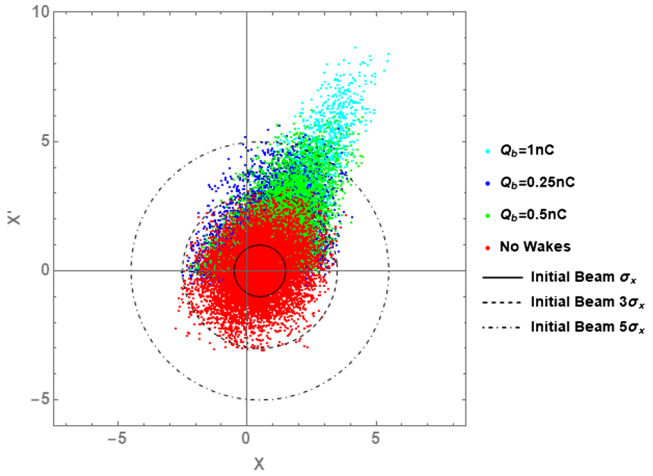

(a) Initial beam offset of $C_x = \sigma_x/2$

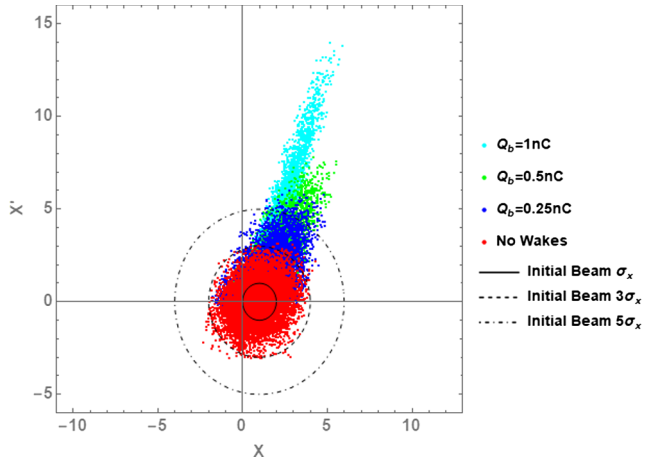

(b) Initial beam offset of $C_x = \sigma_x$

FIG. 42. The normalized phase space $(X, X') = (x/\sqrt{\beta_x \epsilon_x}, (\alpha_x x + \beta_x x')/\sqrt{\epsilon_x \beta_x})$ for beam charge values $Q_b = 0.25$, 0.5 and 1 nC at a beam offsets of $C_x = \sigma_x/2, \sigma_x$ after traveling through 24 rf structures. The normalized coordinates transform the phase space ellipse to the unit circle. Also plotted is the RMS beam width σ_x (solid black), $3\sigma_x$ (dashed black), and $5\sigma_x$ (dot-dashed black).

The evolution of the beam quality parameters are shown in Fig. 43. Assuming an average gradient of the structures of $\langle G \rangle = 80$ MV/m and that a ~180 MeV/c beam enters

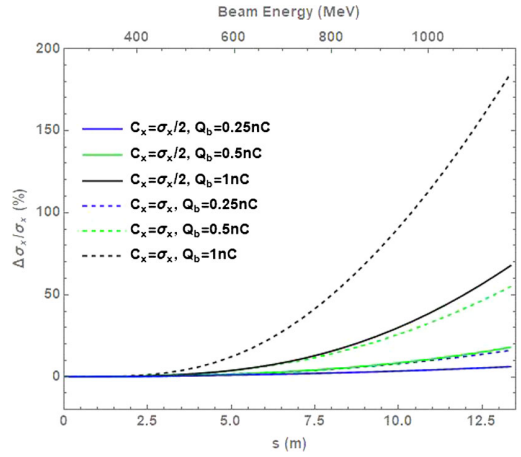

(a) RMS beam size growth of the beam.

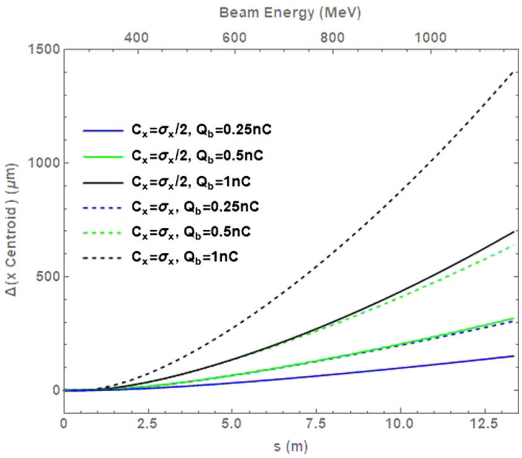

(b) The change in the x centroid of the beam.

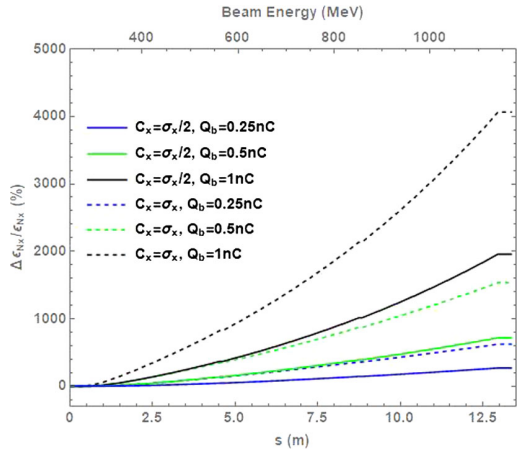

(c) The normalised horizontal emittance of the beam.

FIG. 43. Beam parameters as the beam travels through 24 rf structures for beam charges $Q_b = 0.25$, 0.5 and 1 nC and beam offsets $C_x = \sigma_x/2$ and σ_x. Note that there are 0.4 m of drift space before and after the linac with drift spaces of 2 cell widths between structures and 10 cm between modules. The beam energy is also shown on the top horizontal axis assuming an average structure gradient of $\langle G \rangle = 80$ MV/m.

the XARA system, the design energy of ~1 GeV/c is achieved at $s \approx 10.25$ m downstream from the start of the XARA X-band linacs. This is a conservative design which yields a higher than necessary beam energy but allows for energy losses in a realistic setup. This will ensure that the beam energy is achieved within 3 rf modules which is important due to spatial limitations. This also allows the possibility of reducing the average gradient while still achieving the design beam energy if this becomes necessary in future designs when considering other factors such as breakdown rates or heating effects.

Plotted in red is the result of the ELEGANT simulation for a bunch traveling through the linac but with the longitudinal and transverse wakes neglected. This allows clear comparison of how the wakes effect the bunches for various charges against a reference bunch. Virtually all of the particles in the bunch remain within $3\sigma_x$ of the initial beam for all charges considered with a beam offset of $C_x = \sigma_x/2$. However as the offset is increased to σ_x, more of the bunch falls out of $3\sigma_x$ of the initial beam, with a significant amount of particles lying outside of $5\sigma_x$ for $Q_b = 1$ nC. We also compare the RMS beam size σ_x, the change in the x centroid of the bunch and the normalized emittance growth as the beam traverses the rf linac in Fig. 43. For a bunch charge of $Q_b = 250$ pC and an offset of $C_x = \sigma_z = 0.253$ mm, the normalized emittance growth at the end of the linac is $\Delta\epsilon_{Nx}/\epsilon_{Nx} = 270.8\%$. However, this is a design with no magnetic lattice and aids as a starting point, upon which the emittance growth can be reduced via a future magnetic lattice design to alleviate the wakefields. A main part of the magnetic lattice design would be to include corrector magnets which would recenter the beam in the structure. Recentering the beam as it travels through the structure would significantly reduce the wakefields as misalignments are one of the main contributors to the excitation of transverse wakefields. Further alleviation of the wakefields could be done by including focusing magnetics in the magnetic lattice design. It can be seen in Fig. 43(b) that the transverse wakes move the centroid of the beam away from the initial position of the beam in the direction toward the linac outer walls. As the beam moves further from the electrical axis of the linac, the transverse wakefields have an increasing effect on the bunch. This highlights the importance of beam alignment throughout the structure as centering the beam on the electrical axis will reduce the strength of the transverse wakefields.

VIII. ANALYTICAL EMITTANCE GROWTH

Alongside numerical techniques employed in the ELEGANT code, an analytical formulation of the beam motion can be used to calculate the emittance. In a continuous approximation the transverse motion of a relativistic beam traveling through a misaligned accelerator under the influence of short-range wakefields can be modeled by [32]

$$\frac{1}{\gamma(z')}\frac{\partial}{\partial z'}\left[\gamma(z')\frac{\partial}{\partial z'}x(z',s')\right]+\kappa(s')^2x(z',s') = \epsilon(z')\int_{-\infty}^{s'} w_n(s'-s_1')F(s_1')[x(z',s_1')-d_c(z')]\mathrm{d}s_1', \tag{54}$$

$$\gamma(z') = \gamma_0(1+Gz'), \tag{55}$$

where $z' = z/L$ is the distance measured from the start of the linac normalized to the linac length L; $\gamma(z')$ is the energy parameter along the linac in units of mc^2; $s' = s/l_b$ is the distance measured from behind the head of the bunch normalized to the bunch length l_b; $F(s') = I(s')/I_{\max}$; $I(s')$ and $I_{\max}$ are the instantaneous current and maximum current of the uniform current distribution respectively; $\kappa = kL$ is the betatron focusing wave number k normalized to L; $w_n(s')$ is the normalized transverse wake function; $d_c(z')$ is the lateral displacement of the accelerating sections as a function of location along the linac, $\epsilon(z')$ is the dimensionless coupling strength between the beam and transverse wakes, $\gamma_0 mc^2$ is the energy at the start of the linac and G is the distance required to double the energy. The coupling strength can also be written as $\epsilon(z') = \gamma(0)\epsilon_r/\gamma(z')$ where for short-range wakes,

$$\epsilon_r = \frac{4\pi\epsilon_0 W_0 I_{\max} l_b L^2}{\gamma(0) I_A}, \tag{56}$$

where $I_A \approx 17$ kA is known as the Alfvén current [34], ϵ_0 is the dielectric constant of the vacuum and $W_0 = w(s'=1)$ is the wakefield amplitude. For an accelerated beam the general solution of the equation of motion (54) is given by [32]

$$x(z',s') = \psi(z')^{-1/4}\sum_{n=0}^{\infty}\epsilon_r^n\left\{x_0 h_n(s')j_n(\kappa,\chi) + \left[x_0' g_n(s') + x_0\frac{G}{4}h_n(s')\right]i_n(\kappa,\chi)\right\} - \psi(z')^{-1/4}\sum_{n=0}^{\infty}\epsilon_r^{n+1} f_{n+1}(s')i_n(\kappa,\chi) * \delta_c(\chi), \tag{57}$$

where $\psi(z') = \gamma(z')/\gamma_0$ with $\gamma(z') = \gamma(0)(1+Gz')$; $\delta_c = \psi^{1/4}d_c$; $i_n(\kappa,\chi)$ and $j_n(\kappa,\chi)$ are defined in terms of Bessel functions and circular functions [35,36]; $i_n(\kappa,\chi) * \delta_c(\chi)$ is the convolution between i_n and δ_c and χ is given by

$$\chi = \frac{2z'}{\sqrt{\psi(z')}+1}. \tag{58}$$

In this study, it is assumed that both x_0 and x_0' are time independent. Then $f_n(s') = g_n(s') = h_n(s')$ and is defined by the recursion relation [36]

$$h_{n+1}(s') = \int_{-\infty}^{s'} h_n(s_1')F(s_1')w(s'-s_1')\mathrm{d}s_1', \tag{59}$$

with $h_0(s') = 1$. It is also assumed that $x_0' = 0$ and $d_c = 0$, such that the solution given by Eq. (57) reduces to

$$x(z',s') = \psi(z')^{-1/4}\sum_{n=0}^{\infty}\epsilon_r^n x_0 h_n(s') \times\left\{j_n(\kappa,\chi)+\frac{G}{4}i_n(\kappa,\chi)\right\}. \tag{60}$$

As the XARA beamline currently has no magnetic lattice, it can be considered to have a focusing with an infinite wavelength, or with $\kappa \to 0$. It can be shown that the functions h_n become negligible for higher orders which causes the sum in Eq. (60) to converge quickly. In this study, only terms up to and including $n = 2$ are considered. The normalized wake-function $w_n(s')$ is given by

$$w_n(s') = \frac{w(s')}{W_0}, \tag{61}$$

where $w(s')$ is the transverse wakefunction with normalized coordinates which has been averaged over all cells. For very short bunches the transverse wake can be considered linear across the bunch, i.e., $w_n(s') = s'$, however this will introduces errors in the final results. The normalized wake for the XARA structure and the linear wake are shown in Fig. 44. Once the $x(z',s')$ and $x'(z',s')$ are known the emittance of the bunch can be calculated via

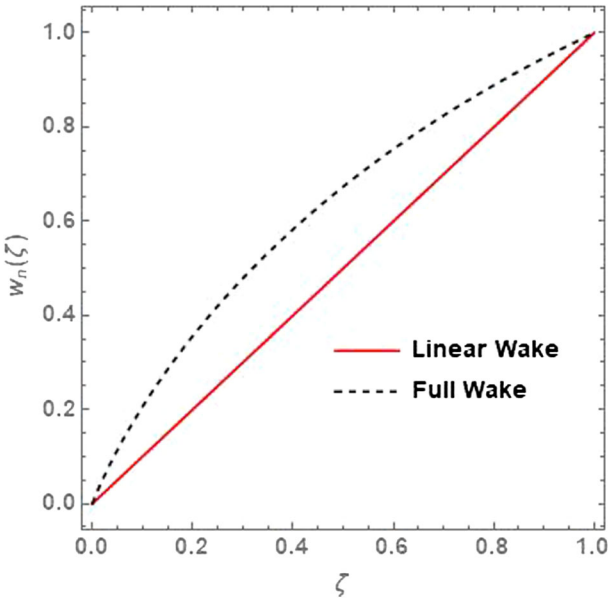

FIG. 44. Comparison between the normalized transverse wake-function for the XARA structure and the linear approximation of the wake.

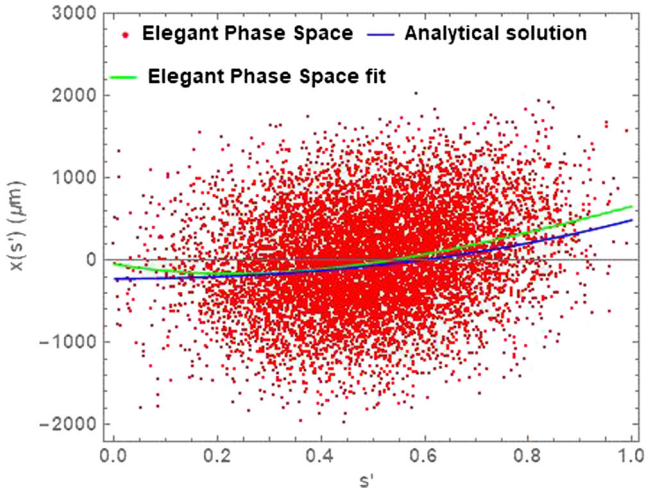

FIG. 45. Comparison of $x(z'=1,s')$ between the ELEGANT tracking code results and the analytical formulation for a bunch which has traveled through the 24 rf structures of XARA. Shown in red is the raw phase space of the bunch, a fit of which is given in solid green. The analytical result is shown in blue.

$$\epsilon(z') = \sqrt{\langle x(z',s')^2\rangle\langle x'(z',s')^2\rangle - \langle x(z',s')x'(z',s')\rangle^2}, \tag{62}$$

where the averages are now given by

$$\langle x(z',s')\rangle = \int_0^1 x(z',s')\mathrm{d}s'. \tag{63}$$

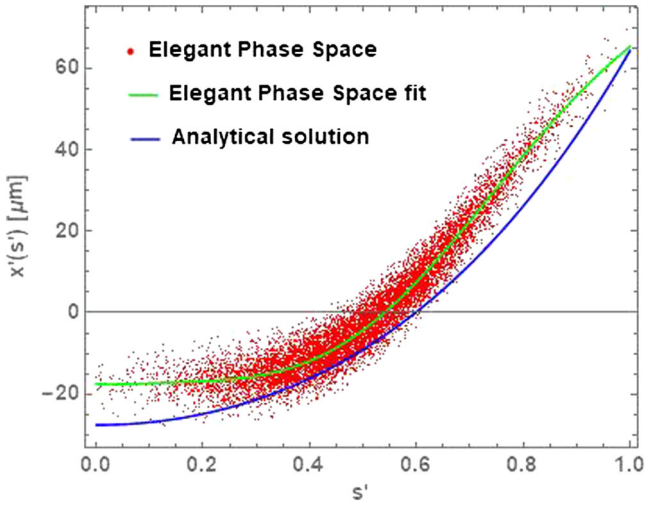

FIG. 46. Comparison of $x'(z'=1,s')$ between the ELEGANT tracking code results and the analytical formulation for a bunch which has traveled through the 24 rf structures of XARA. Shown in red is the raw phase space of the bunch, a fit of which is given in solid green. The analytical result is shown in blue.

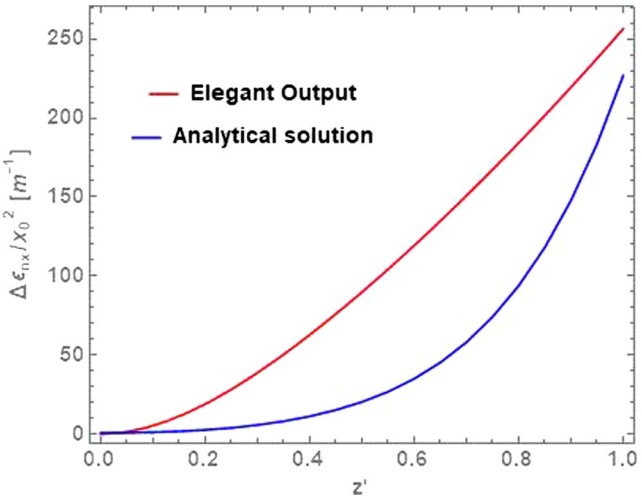

FIG. 47. Comparison of the normalized emittance growth where $\epsilon(z')$ given by Eq. (62) between the ELEGANT tracking code results and the analytical formulation for a bunch which has traveled through the 24 rf structures of XARA. Shown in red is the normalized emittance calculated via ELEGANT. The analytical result is shown in blue.

Comparisons between the ELEGANT tracking code and the analytical formulation have been compared in Figs. 45 and 46 for an initial offset of $\sigma_x/2 = 0.253$ mm, showing x and x' respectively at the end of the linac ($z'=1$). The resultant normalized emittance growth of the bunch is shown in Fig. 47. The analytical results show generally good agreement with the ELEGANT results with a $\sim$12% difference in the calculated normalized emittance at the end of the linac $z'=1$. In the ELEGANT simulations a cutoff of $3\sigma_z$ was used, resulting in a bunch length $l_b = 0.6$ mm. The discrepancies between the ELEGANT and analytical results may be explained by the fact that a flat current profile and a linear wakefield are assumed in the analytical model. However due to the short bunch lengths when compared to the length of the cells, these approximations are not unreasonable and the analytical formulation gives a good representation of the normalized emittance growth. This gives good reliability for the ELEGANT simulations performed for the XARA structure as similar results can be achieved analytically with reasonable approximations.

IX. CONCLUSION

In this paper, a solid framework has been created to create a base design for an X-band linac which would be used in the XARA upgrade of the existing CLARA accelerator. Optimizations of the effective shunt impedance, the external quality factor of a SLED rf setup, and the modified Poynting vector were done using a numerical tool based on the physics of an output rf pulse traveling through a structure. Both linear and Gaussian tapered irises were considered with a Gaussian taper ultimately being chosen as it creates a reduced wakefield which is beneficial for a

future potential multibunch regime. Wakefield analysis was carried out by considering the uncoupled transverse wakefield in the structure and studying the initial fall off. The usefulness of an analytical expression for the linear and Gaussian uncoupled wakefields was explored by considering the Fourier Transform of the quantity $K\mathrm{d}n/\mathrm{d}\omega$. It was found that these expressions can be useful for a range of linear tapers, standard deviations and frequency spreads at small distances, and allow for rapid calculation for the uncoupled wakefield which will allow the wakefields of future designs to be yielded quickly. An optimal design with $\sigma = 0.5$ GHz, $\Delta\omega/2\pi = 1.5$ GHz and $L = 0.5$ m was chosen as a compromise between these parameters. Once a design had been decided, the short-range transverse and longitudinal wakefields were calculated via an impedance field-matching technique [28] and executed by a FORTRAN code [27]. Fitted wakefield functions were found which depend on the iris radii, cell gap and length of the individual cells and is valid over a range of these parameters. The numerical and fitted wakes were then calculated for 7 representative cells for an example XARA structure. These results have been benchmarked by calculating the bunch wakes via a convolution of the point-charge wake with the Gaussian charge distribution of the bunch. The bunch wakes were then compared to simulations carried out in the wakefield simulation programs ABCI and ECHO2D with good agreement for both the longitudinal and transverse wakefields. The average wakes were also found for the short-range wakefields, as the average wake of the individual cells gives a good approximation of the wakefield of the whole structure. The forms of the wakefields found will be utilized in any future designs for the XARA structure and will make the general design process more straightforward. ELEGANT simulations were then carried out to study how the beam properties evolve as a $\sigma_z = 0.1$ mm electron bunch travels through a single rf cavity structure and a lattice of 24 rf cavities. These beam dynamics simulations prescribe a bunch charge limit which is restricted by an allowable emittance dilution. The behavior of the bunch with offset also gives a limit to the allowed misalignment of the rf structures of the XARA machine. These ELEGANT results have been compared to an analytical formulation of the emittance growth for a bunch charge of $Q_b = 250$ pC and a beam offset of $C_x = \sigma_z = 0.253$ mm, where results within $\sim$12% at the end of the linac were achieved. The results do not agree well before the end of the linac and this is potentially due to a combination of the assumptions made by the analytical description and the first-order techniques used by ELEGANT. The normalized emittance growth at the end of the XARA linac as calculated via ELEGANT is $\Delta\epsilon_{Nx}/\epsilon_{Nx} = 270.8\%$.

ACKNOWLEDGMENTS

M. S. S. would like to thank Prof. Jim Clarke for his helpful comments and feedback in this work. M. S. S. would also like to thank Dr. James Jones for his assistance in setting up the ELEGANT and beam dynamics simulations and for essential discussions which propelled the speed of this study significantly. M. S. S. and R. M. J. were supported by the STFC grant No. ST/V001612/1.

[1] J. Clarke *et al.*, The Conceptual Design of CLARA, A Novel FEL Test Facility for Ultrashort Pulse Generation, in *4th International Particle Accelerator Conference* (JACoW, Geneva, 2013), p. TUPEA058.

[2] D. Dunning, L. Cowie, and J. Jones, "XARA: X-Band Accelerator for Research and Applications," in *39th International Free Electron Laser Conference*, p. THP066, 2019, https://inspirehep.net/literature/1780326.

[3] J. Marangos, UK-XFEL draft science case, 2020, https://www.clf.stfc.ac.uk/Pages/UK-XFEL-science-case.aspx.

[4] D. Angal-Kalinin *et al.*, Design, specifications, and first beam measurements of the compact linear accelerator for research and applications front end, Phys. Rev. Accel. Beams **23**, 044801 (2020).

[5] G. D'Auria *et al.*, CompactLight design study, in *10th International Particle Accelerator Conference* (JACoW, Geneva, 2019.

[6] M. Diomede *et al.*, Preliminary rf design of an X-band linac for the EuPRAXIA@SPARC_LAB project, https://inspirehep.net/literature/1645691.

[7] Z. Farkas, H. Hoag, G. Loew, and P. B. Wilson, SLED: A Method of Doubling SLAC's Energy.," in *9th International Conference on High-Energy Accelerators* (1974), pp. 576–583, https://inspirehep.net/literature/94052.

[8] A. A. Mondelli, D. P. Chernin, A. T. Drobot, M. Reiser, and V. Granatstein, Frequency scaling of rf linacs, IEEE Trans. Nucl. Sci. **32**, 3157 (1985).

[9] R. M. Jones, C. E. Adolphsen, J. W. Wang, and Z. Li, Wakefield damping in a pair of x-band accelerators for linear colliders, Phys. Rev. ST Accel. Beams **9**, 102001 (2006).

[10] R. M. Jones, Wakefield suppression in high gradient linacs for lepton linear colliders, Phys. Rev. ST Accel. Beams **12**, 104801 (2009).

[11] M. Dehler, I. Wilson, and W. Wuensch, A tapered damped accelerating structure for CLIC, Report No. CERN-PS-98-40-LP", 1998.

[12] Ansys HFSS Electronics Desktop, https://www.ansys.com/products/electronics/ansys-hfss.

[13] M. Borland, elegant: A Flexible SDDS-Compliant Code for Accelerator Simulation, in *6th International Computational Accelerator Physics Conference (ICAP 2000)*, 2000.

[14] M. Diomede, High-gradient structures and rf systems for high-brightness electron linacs, Ph.D. thesis, Rome U., 2020.

[15] A. Grudiev, S. Calatroni, and W. Wuensch, New local field quantity describing the high gradient limit of accelerating structures, Phys. Rev. ST Accel. Beams **12**, 102001 (2009); **14**, 099902 (2011).

[16] M. Vretenar, Linear accelerators, Mar 2013. Comments: 25 pages, contribution to the CAS—CERN Accelerator

School: Course on High Power Hadron Machines; 24 May —2 Jun 2011, Bilbao, Spain, https://inspirehep.net/literature/1416210.

[17] L. Carver, Studies on multi-harmonic collinear accelerating structures for high gradient Applications, Ph.D. thesis, The University of Manchester, 2016.

[18] L. R. Carver, R. M. Jones, Y. Jiang, and J. L. Hirshfield, Longitudinal stability in multiharmonic standing wave linacs, Phys. Rev. Accel. Beams **19**, 094001 (2016).

[19] B. Zotter and K. Bane, Transverse modes in periodic cylindrical cavities, Experientia **40**, 581 (1980), https://inspirehep.net/literature/154952.

[20] W. R. Inc., Mathematica, Version 12.2. Champaign, IL, 2020.

[21] A. Lunin, V. Yakovlev, and A. Grudiev, Analytical solutions for transient and steady state beam loading in arbitrary traveling wave accelerating structures, Phys. Rev. ST Accel. Beams **14**, 052001 (2011).

[22] R. M. Jones, V. A. Dolgashev, and J. W. Wang, Dispersion and energy compensation in high-gradient linacs for lepton colliders, Phys. Rev. ST Accel. Beams **12**, 051001 (2009).

[23] K. Bane and R. L. Gluckstern, The transverse wake field of a detuned x band accelerator structure, Part. Accel. **42**, 123 (1993), https://inspirehep.net/literature/333150.

[24] J. A. Clarke *et al.*, CLARA conceptual design report, J. Instrum. **9**, T05001 (2014).

[25] K. L. Bane, Short range dipole wakefields in accelerating structures for the NLC, Report No. SLAC-PUB-9663, LCC-0116, 2003.

[26] R. Gluckstern, Longitudinal impedance of a periodic structure at high frequency, Phys. Rev. D **39**, 2780 (1989).

[27] K. Yokoya, Short-range impedance., in *4th Advanced ICFA Beam Dynamics Workshop on Collective Effects in Short Bunches*, pp. 142–150, 2 1991.

[28] H. Henke, Impedances of a set of cylindrical resonators with beam pipes, Part. Accel. **25**, 183 (1990), https://inspirehep.net/literature/251756.

[29] A. Grudiev, Very short-range wakefields in strongly tapered disk-loaded waveguide structures, Phys. Rev. ST Accel. Beams **15**, 121001 (2012).

[30] Y. H. Chin, ABCI, https://inspirehep.net/literature/261093.

[31] T. Weiland, A discretization model for the solution of Maxwell's equations for six-component fields, *Archiv Elektronik und Uebertragungstechnik* (1977), vol. 31, pp. 116–120, https://ui.adsabs.harvard.edu/abs/1977ArElU..31..116W/abstract.

[32] P. Craievich and S. Di Mitri, Emittance growth due to short-range transverse wakefields in the FERMI linac, 01 2005, https://inspirehep.net/literature/703546.

[33] M. G. Minty and F. Zimmermann, Beam techniques: Beam control and manipulation, in *U.S. Particle Accelerator School (USPAS 1999)*, 1999, https://inspirehep.net/literature/518758.

[34] P. Craievich, Short-range longitudinal and transverse wakefield effects in FERMI@Elettra FEL project, PhD thesis, Technische Universiteit Eindhoven, 2010.

[35] J. R. Delayen, Cumulative beam breakup in linear accelerators with arbitrary beam current profile, Phys. Rev. ST Accel. Beams **6**, 084402 (2003).

[36] J. R. Delayen, Cumulative beam breakup in linear accelerators with random displacement of cavities and focusing elements, Phys. Rev. ST Accel. Beams **7**, 074402 (2004).